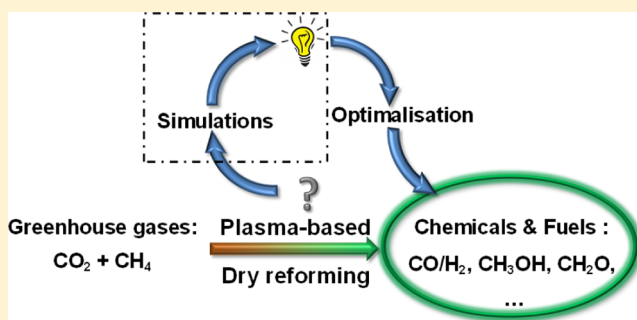


Plasma-Based Dry Reforming: A Computational Study Ranging from the Nanoseconds to Seconds Time Scale

Ramses Snoeckx,[†] Robby Aerts,[†] Xin Tu,[‡] and Annemie Bogaerts^{*,†}[†]Research group PLASMANT, University of Antwerp, Department of Chemistry, Universiteitsplein 1, B-2610 Wilrijk-Antwerp, Belgium[‡]Department of Electrical Engineering and Electronics, University of Liverpool, Liverpool L69 3GJ, United Kingdom**S** Supporting Information

ABSTRACT: We present a computational study for the conversion of CH₄ and CO₂ into value-added chemicals, i.e., the so-called “dry reforming of methane”, in a dielectric barrier discharge reactor. A zero-dimensional chemical kinetics model is applied to study the plasma chemistry in a 1:1 CH₄/CO₂ mixture. The calculations are first performed for one microdischarge pulse and its afterglow, to study in detail the chemical pathways of the conversion. Subsequently, long time-scale simulations are carried out, corresponding to real residence times in the plasma, assuming a large number of consecutive microdischarge pulses, to mimic the conditions of the filamentary discharge regime in a dielectric barrier discharge (DBD) reactor. The conversion of CH₄ and CO₂ as well as the selectivity of the formed products and the energy cost and energy efficiency of the process are calculated and compared to experiments for a range of different powers and gas flows, and reasonable agreement is reached.



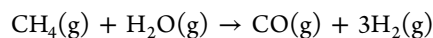
1. INTRODUCTION

The conversion of greenhouse gases (mainly CO₂ and CH₄) into value-added chemicals or new fuels is considered as one of the main challenges for the 21st century (see, e.g., refs 1–3). By doing so, the greenhouse gases can constitute an alternative for petroleum, which will become less available and therefore more expensive. Moreover, this conversion process can be considered to fit in the revolutionary “cradle-to-cradle” concept^{4,5} because the waste (greenhouse gases) can be converted into a new feedstock (raw materials for the chemical industry).

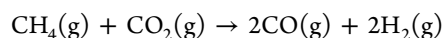
The conversion process of CO₂ and CH₄ is, however, not straightforward. Indeed, CO₂ is a highly oxidated, thermodynamically stable molecule, and its use in redox reactions requires highly energetic reactants or electro-reducing processes.⁶ CH₄ is, due to its chemical inertness, currently a highly underutilized source for the production of value-added chemicals. A direct (thermal) synthesis route for hydrocarbons from CH₄ is technically not possible, and the conventional indirect methods are characterized by low yields and require a high energy input.⁷ For instance, the production of methanol (CH₃OH) out of CH₄ can occur through the so-called steam-methane-reforming (SMR), producing syngas (i.e., a mixture of CO and H₂), which is further converted by a second catalytic process into methanol. This is, however, an inefficient process.

Nevertheless, the reforming of methane into syngas is gaining increased attention worldwide,⁸ due to the versatility of syngas for the production of many fuels and chemicals, such as methanol, but also Fischer–Tropsch fuels, H₂, ethanol,

dimethyl ether, ...⁹ There exist six different types of reforming processes, which all produce syngas in different H₂/CO ratios (also called the syngas ratio); this ratio is important since different end products require different ratios.¹⁰ The two most important reforming processes are the SMR and the so-called dry reforming of methane (DRM), where CO₂ is the coreactant instead of steam. Both processes are carried out at high temperatures (700–1000 °C and 600–900 °C, respectively) in the presence of a Ni-containing catalyst. The SMR process, i.e.,



is already commonly used worldwide, for instance, in the fertilizer industry (where H₂ is used for the ammonia production) and in the gas industry (where it is responsible for 95% of the worldwide production of H₂).¹¹ The process, however, is strongly endothermic, and often (energy-intensive) post-treatments of the products are needed, depending on the desired syngas application. Hence, a large amount of greenhouse gases will be produced for the energy production required for this process, thereby significantly limiting the attractiveness of this technique.¹² The DRM process, i.e.,

**Received:** December 4, 2012**Revised:** February 13, 2013**Published:** February 18, 2013

is, as mentioned above, carried out at high temperatures by means of a catalyst, typically containing Ni, Co, precious metals, or Mo₂C as the active phase.¹³ This reaction is even 20% more endothermic than the SMR reaction,^{12,13} but taking a brief look at the reaction equation reveals that the two most important greenhouse gases are converted at the same time.

On the industrial scale the DRM is carried out most efficiently at 700 °C, reaching thermodynamic equilibrium conversions of CH₄ and CO₂ of 72% and 82%, respectively.¹⁴ For the reaction between 1 kmol CH₄ and 1 kmol CO₂ at 700 °C, 260 MJ energy is needed, and at least an additional 70 MJ is required to bring the gas flow to this temperature. This means that at least about 330 MJ energy is required for this process. This results in an energy input of at least about 3.42 eV per molecule and a corresponding maximum theoretical energy efficiency of 58%. These values are important, as they will be the benchmark for the results obtained in the present study. It is important to keep in mind that when talking about energy efficiency in this study we always mean the theoretical energy efficiency. For instance, to determine the total energy efficiency of the classical process one would also need to account for the thermal efficiency of the heaters, which depends on the type of heater used, the type of fuel used, and the use of heat recovery systems. Likewise, for the plasma process, one needs to take into account the energy losses that occur at the level of the generator, the transformer, and the plasma reactor.

One of the largest problems of the DRM process is the high amount of carbon deposition at the catalyst material, i.e., much higher than with SMR, giving rise to catalyst poisoning.^{12,13} A lot of research is going on to search for the optimum catalyst materials (e.g., refs 14–16). On the other hand, in recent years there is also growing interest for alternative reforming techniques, based on milder reaction conditions, such as plasma reformers. Both thermal and nonthermal plasma reformers have already been developed.^{17–21} Another growing field of interest is the combination of plasma and catalysis, so-called plasma catalysis, which seems to be promising, because it combines the selectivity of catalysis with the capability of plasmas to induce thermodynamically unfavorable reactions.^{22–25} Indeed, the inert molecules (CH₄, CO₂) are “activated” by the plasma (i.e., reactive species, such as radicals, are formed), whereas the catalyst makes sure that the reactive components selectively recombine into the desired end-products.

The central research question is, however, whether plasma catalysis can yield a valuable alternative to the existing inefficient thermal processes. Due to the complexity of the entire process, this question cannot be readily answered and requires a multidisciplinary and integrated approach, to be conducted in a concerted action by plasma physicists, process engineers, chemists, material scientists, ... Therefore, it is necessary to first seek answers to some other questions related to specific aspects of this process. Indeed, an important condition for obtaining progress in this field is to obtain a better understanding of the underlying chemical and physical processes in the plasma, even without a catalyst. Nowadays, a lot of research in this domain is still based on assumptions without a good understanding of the ongoing plasma processes. Indeed, several interesting experiments have already been performed for the dry reforming of methane with dielectric barrier discharges (DBDs),^{17,26–37} but there is a clear need for modeling, to better understand and interpret these experiments.

In this paper, we will study the plasma-based dry reforming process in a DBD reactor, by means of computer simulations. In our investigation we will make use of a zero-dimensional (0D) chemical kinetics model. Simplified calculations for this plasma chemistry have already been performed,^{27,32–34} but they were all based on simplified kinetics and without a (good) description of the filamentary discharge regime. Therefore, we will carry out an extensive study of the reaction chemistry while mimicking the filamentary discharge regime. More specifically, we will investigate the plasma chemistry in one microdischarge pulse and its afterglow, which corresponds to one filament in a DBD, as well as the impact of several consecutive discharge pulses. Subsequently, the model will be applied to long time scales, corresponding to the typical residence times of the gases in a DBD reactor, to calculate the conversion of CH₄ and CO₂, the selectivity of the reaction products, and the energy cost and energy efficiency of the process. These long time-scale simulations will be compared with experiments to validate the model.

2. DESCRIPTION OF THE MODEL

2.1. 0D Chemical Kinetics Model. We make use of a 0D chemical kinetics model, called *Global_kin*, developed by Kushner and co-workers,^{38,39} to describe the plasma chemistry. This means that the plasma is treated as a “batch reactor”, with a uniform species density and neglecting species transport. The model consists of three basic modules, i.e., a 0D plasma chemistry module, a Boltzmann equation module, and a circuit module. In this work, only the first two modules are used. The time evolution of the species densities is calculated, based on production and loss processes, as defined by the chemical reactions

$$\frac{dn_i}{dt} = \sum_j \{ (a_{ij}^{(2)} - a_{ij}^{(1)}) k_j \prod_l n_l^{a_{lj}^{(1)}} \}$$

$a_{ij}^{(1)}$ and $a_{ij}^{(2)}$ are the stoichiometric coefficients of species i , at the left and right-hand side of the reaction j , respectively. n_l is the species density at the left-hand side of the reaction, and k_j is the rate coefficient of reaction j . The rate coefficient of the heavy particle reactions depends on gas temperature and is calculated by Arrhenius equations. The rate coefficient for the electron impact reactions is a function of the electron temperature and is calculated in the Boltzmann equation module and tabulated for a range of E/n values.^{38,39} The electron temperature is calculated with the following energy balance equation

$$\frac{d}{dt} \left(\frac{3}{2} n_e k_B T_e \right) = \bar{j} \cdot \bar{E} - \sum_i \frac{3}{2} n_e \nu_{mi} \left(\frac{2m_e}{M_i} \right) k_B (T_e - T_i) + \sum_l n_e k_l N_l \Delta \epsilon_l$$

n_e is the electron density; T_e is the electron temperature; \bar{j} and \bar{E} are the current density and electric field in the plasma; ν_{mi} is the electron momentum transfer collision frequency with species i ; m_e is the electron mass; and M_i and T_i are the mass and temperature of species i . k_j is the reaction rate coefficient of electron impact reaction j ; N_l is the density of species l ; and $\Delta \epsilon_l$ is the change in electron energy (hence a negative value for electron energy loss). The first term at the right-hand side of this equation is the energy gain due to Joule heating, whereas the second and third terms denote the energy loss due to elastic

and inelastic collisions, respectively. As the model is 0D, we do not know the electric field distribution in the plasma; therefore, the Joule heating is calculated as the applied power density. More information about this model can be found in refs 38 and 39.

2.2. Plasma Chemistry Included in the Model. The plasma chemistry described in the model is based on the chemistry set developed by De Bie et al.⁴⁰ However, some species and chemical reactions were removed from the model, as they were found to be negligible at the conditions under study. The species included in the present model are listed in Table 1. They react with each other in 121 electron impact

Table 1. List of Species Included in the Model for the CH₄/CO₂ Gas Mixture^a

molecules	charged species	radicals	excited species
CH ₄	CH ₃ ⁺ , CH ₄ ⁺ , CH ₃ ⁺ , CH ₂ ⁺ , CH ⁺	CH ₃ , CH ₂ , CH, C	CH ₄ [*]
C ₂ H ₆ , C ₂ H ₄ , C ₂ H ₂	C ₂ H ₆ ⁺ , C ₂ H ₅ ⁺ , C ₂ H ₄ ⁺ , C ₂ H ₃ ⁺ , C ₂ H ₂ ⁺	C ₂ H ₅ , C ₂ H ₃ , C ₂ H	C ₂ H ₆ [*] , C ₂ H ₄ [*] , C ₂ H ₂ [*]
C ₃ H ₈ , C ₃ H ₆ , C ₄ H ₂		C ₃ H ₇	C ₃ H ₈ [*]
H ₂		H	H ₂ [*]
O ₂	O ₂ ⁺ , O ⁻	O	O [*]
CO ₂ , CO	CO ₂ ⁺		CO ₂ [*] , CO [*]
H ₂ O, H ₂ O ₂	H ₃ O ⁺ , OH ⁻	OH, HO ₂	H ₂ O [*]
CH ₃ O, CH ₃ OH	electrons	CHO, CH ₂ OH, CH ₃ O	
CH ₃ CHO, CH ₂ CO		C ₂ HO, CH ₃ CO, CH ₂ CHO, C ₂ H ₃ O ₂	

^aNote: The excited species are only included in the model to describe the energy loss processes, and they are not treated as separate species.

reactions, 87 ion reactions, and 290 neutral reactions, which are listed in the Supporting Information, together with their corresponding rate coefficients and the references where these data were adopted from.

2.3. Description of the Power Deposition in the Filamentary DBD Plasma. In most reactive gases, a DBD typically occurs in the so-called filamentary regime, consisting of a large number of independent microdischarge filaments, with a duration in the nanosecond range, typically around 1–100 ns.⁴¹ The current pulses of these microdischarges appear with a certain frequency, corresponding to twice the applied frequency (see Figure 1). In these microdischarges a large fraction of the electron energy is used for excitation, dissociation, and ionization of the molecules and therefore to initiate the chemical reactions. This is the reason why these microdischarges are of prime importance for a realistic description of the reaction chemistry.

We cannot treat the spatial aspect of filament formation in our 0D model, but we can mimic the filamentary behavior by simulating a large number of microdischarge pulses as a function of time. From Figure 1 it is clear that several microdischarge pulses occur per half cycle. Assuming a typical applied frequency of 35 kHz (as used in the experiments²⁶ for validation), this corresponds to a duration of 14 μs for each half cycle. Unfortunately, the number of microdischarge pulses that each gas molecule will pass when traveling through the DBD reactor is not known. If we assume that each molecule passes one microdischarge each half cycle, this would correspond to 70,000 microdischarge pulses per second. That will be our

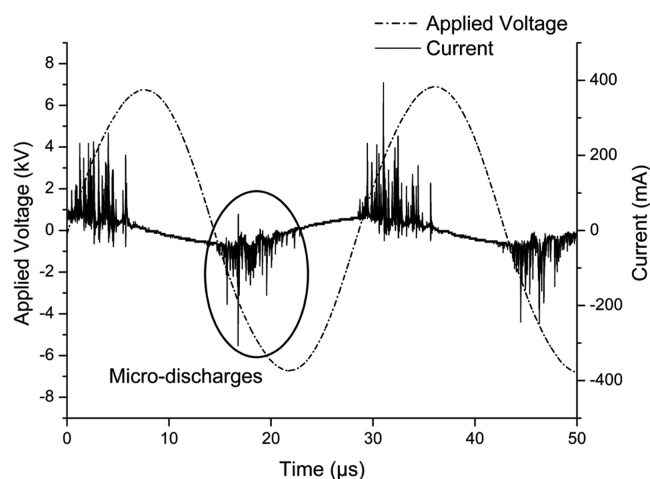


Figure 1. Applied voltage (left axis) and resulting current (right axis) as a function of time, for a DBD of 35 kHz and 50 W. The microdischarge pulses (filaments) are indicated.

starting assumption in the long time-scale simulations presented in Section 3. Furthermore, as we do not know the exact time evolution of a microdischarge, we simply assume a triangular pulse, with a duration of 30 ns. The maximum power of the pulse is chosen in such a manner that the specific energy input (SEI) can be compared with experimental results²⁶ for validation (see below).

First we will investigate in detail the behavior of one microdischarge pulse and its afterglow. Subsequently, the accumulation effect of several microdischarge pulses will be studied, and finally real time-scale simulations will be carried out, with a large number (in the order of hundreds or thousands) of microdischarge pulses per second, to calculate the conversion of CH₄ and CO₂, the selectivity of the products, and the energy cost and energy efficiency of the process. The calculations will be performed for a 1:1 ratio of CH₄/CO₂, to allow a direct comparison and validation with the experimental data obtained in ref 26.

3. CALCULATED BEHAVIOR OF ONE MICRODISCHARGE PULSE AND ITS AFTERGLOW

3.1. Power Deposition, Electron Density, and Temperature. Figure 2 illustrates the applied power deposition (P), as well as the calculated electron density (N_e) and electron temperature (T_e), as a function of time, for one microdischarge pulse. At $t = 3 \times 10^{-8}$ s, a triangular pulse of 30 ns is applied, assuming a maximum power deposition of 1.5×10^5 W/cm³ (Figure 2(a)). The electron density (Figure 2(b)) follows the same profile as the power deposition, which is logical as the power is transferred to the electrons, which are heated and give rise to electron impact ionization, creating more electrons. However, the electron density shows a slower decay in the afterglow, indicating that some electrons have a somewhat longer lifetime, or can still be created in the afterglow by heavy-particle reactions. The electron temperature is illustrated in Figure 2(c). It shows an initial maximum before the start of the pulse, which is an artifact of the simulations, as the model seems first to overestimate, before converging to the real value of the electron temperature. However, this artifact does not affect the calculation results because it occurs in the first nanoseconds, where the electron density is still negligible, so it cannot give rise to reactions with the gas molecules. As soon as

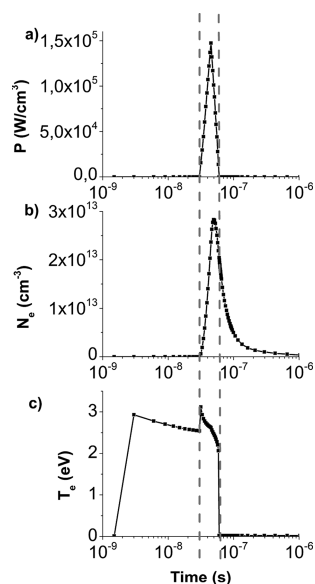


Figure 2. Applied power deposition (a) and calculated electron density (b) and electron temperature (c), as a function of time for one pulse and afterglow. The gray dashed lines indicate the start and the end of the microdischarge pulse.

the discharge pulse starts, the electron temperature reaches a maximum, which is real, because the electrons are heated by the electric field. Upon termination of the pulse, the electron temperature drops to 0.05 eV. The maximum electron temperature is around 2.5–3 eV, which corresponds well with experimental data from the literature.^{17,41,42} The maximum electron density is about $3 \times 10^{13} \text{ cm}^{-3}$, which is in the same order of magnitude as experimental values ($\sim 10^{12} - 10^{14} \text{ cm}^{-3}$).^{17,41,42} We may therefore conclude that the power deposition assumed for this single discharge pulse correlates well with typical DBD conditions, so that the chemical behavior of the CH_4/CO_2 mixture can be described in a realistic way.

3.2. Densities of the Plasma Species. (a). *Overall Densities.* As illustrated above, electrons are created upon the start of the pulse, and they can give rise to collisions with the gas molecules, thereby forming radicals and ions, as is clear from Figure 3. During the pulse, the density of the molecules

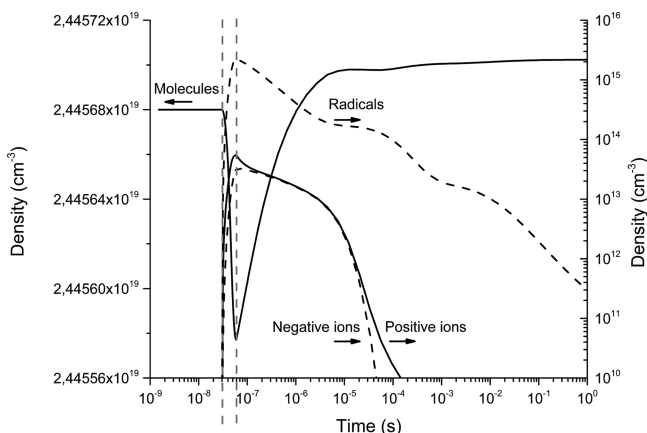


Figure 3. Calculated densities of the molecules (left axis) and of the radicals and positive and negative ions (right axis), as a function of time during one pulse and afterglow. The gray dashed lines indicate the start and the end of the microdischarge pulse.

drops slightly (see left axis), whereas the densities of the ions, and especially of the radicals, increase by several orders of magnitude (see right axis). Comparing the ion and radical densities, it is clear that the electron impact reactions mainly create radicals and that electron impact dissociation will be the dominant loss mechanism for CH_4 and CO_2 . In the afterglow, the molecule density rises again, whereas the densities of ions and radicals drop because they recombine again with the formation of stable molecules. This illustrates that the plasma chemistry is completely different in the afterglow, due to the absence of an electric field. Indeed, the electrons disappear (see Figure 2 above), and the chemistry is dominated by heavy particle reactions. The ions have disappeared after 100 μs , whereas the radicals reach a kind of steady state at 5 μs but drop further after 100 μs . Note that we assume an afterglow of 1 s here, which probably does not correspond to reality (see Section 2.3 above); hence, the accumulation effect of consecutive pulses needs to be examined as well, and these results will be presented in Section 4 below.

(b). *Densities of CH_4 and CO_2 .* The densities of CH_4 and CO_2 are plotted as a function of time during one pulse and afterglow in Figure 4. During the pulse, the dissociation of CH_4

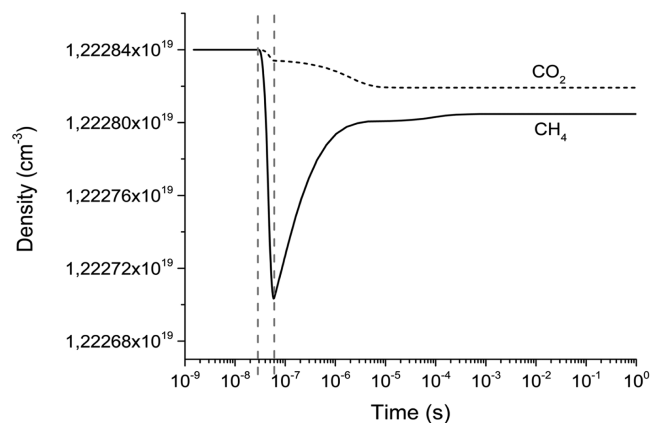


Figure 4. Calculated densities of CH_4 and CO_2 , as a function of time during one pulse and afterglow. The gray dashed lines indicate the start and the end of the microdischarge pulse.

is much more pronounced, which can be attributed to a more efficient dissociation by electron impact for CH_4 or to a competition with production processes for CO_2 during the pulse. The exact reason will be elucidated below, in Section 3.3. In the afterglow, however, nearly 74% of the dissociated CH_4 is formed again, due to the recombination of CH_3 and H . The CO_2 dissociation, on the other hand, continues in the afterglow, but after 10 μs an equilibrium is reached between production and loss of CO_2 . Our calculations predict that ca. 22% of the CO_2 dissociation occurs during the pulse and is attributed to electron impact dissociation, whereas 78% takes place in the afterglow and is mainly due to reactions of CO_2 with CH_2 radicals. Nevertheless, overall the conversion of CH_4 is still a factor of 2 higher than for CO_2 . After 10 μs , the CH_4 and CO_2 densities reach a steady state value, indicating that the production and/or loss processes compensate each other or have become all negligible.

(c). *Densities of the Important Molecules.* Figure 5 presents the time evolution of the most important molecule densities, formed out of CH_4 and CO_2 . The higher hydrocarbon molecules, C_2H_6 , C_2H_4 , C_2H_2 , C_3H_8 , and C_3H_6 , are shown in

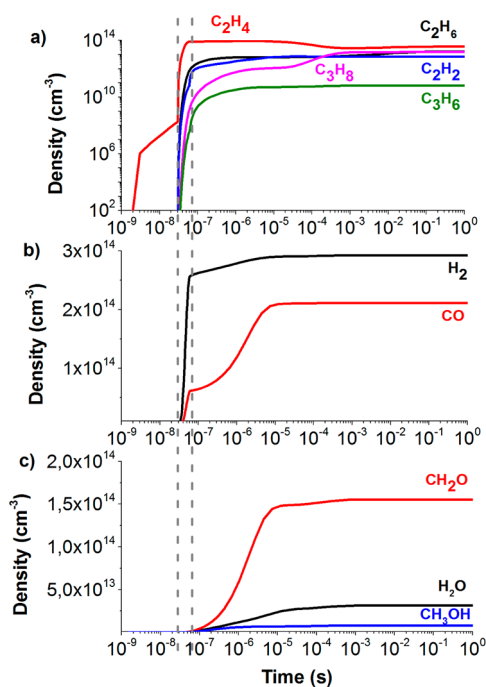


Figure 5. Calculated densities of the most important molecules formed in the plasma, i.e., higher hydrocarbons (a), syngas components (b), and H_2O and oxygenated products (c), as a function of time during one pulse and afterglow. The gray dashed lines indicate the start and the end of the microdischarge pulse.

Figure 5(a). Note that the considerable density of C_2H_4 before the pulse is again an artifact of the simulations, due to some overestimated starting values; however, it has no influence on the results because it happens before the pulse starts, and the density is 11 orders of magnitude lower than the CH_4 and CO_2 densities. Once the pulse starts, we notice a significant increase in density, over more than 10 orders of magnitude for the hydrocarbon densities. There is, however, some difference between the different hydrocarbons; i.e., the densities of C_2H_6 , C_2H_4 , and C_2H_2 rise instantaneously upon start of the pulse, whereas the rise in densities of C_3H_8 and C_3H_6 exhibits some delay. This is because the latter molecules are created only after some intermediate products are formed (see Section 3.3 below). In the afterglow, some densities continue to grow, whereas other densities drop slightly, indicating a conversion from lower to higher hydrocarbons. After about 1 ms, all densities reach steady state values.

The densities of the syngas components, CO and H_2 , are depicted in Figure 5(b). The H_2/CO ratio during the pulse is ~ 4 . However, in the afterglow, the CO density increases more drastically than the H_2 density, due to the continued dissociation of CO_2 (see above), and the final H_2/CO ratio, after about 5 μs , is ~ 1.4 . This ratio is interesting for several industrial applications like for example the dimethyl ether production and Fischer–Tropsch synthesis.⁴³

Finally, Figure 5(c) illustrates the densities of H_2O and of the two most important oxygenated products, i.e., formaldehyde (CH_2O) and methanol (CH_3OH). The latter two molecules are even more important than syngas for the chemical industry, as they are bulk chemicals that are largely consumed worldwide for a large number of industrial syntheses.⁴⁴ Hence it would be beneficial if they could be produced directly from the CH_4/CO_2 gas mixture. It is clear that these species are mainly formed

in the afterglow and not by electron impact reactions during the pulse. The formaldehyde density is only a factor of 2 lower than the densities of the syngas components, whereas the methanol density is still 1 order of magnitude lower. The most important production process for formaldehyde is the reaction



whereas methanol is mainly formed by



These molecules only reach steady state densities after ca. 1 ms.

(d). *Densities of the Important Radicals and Ions.* The time evolution of the most important radical and ion densities is illustrated in Figure 6. In general, the radicals (see Figure

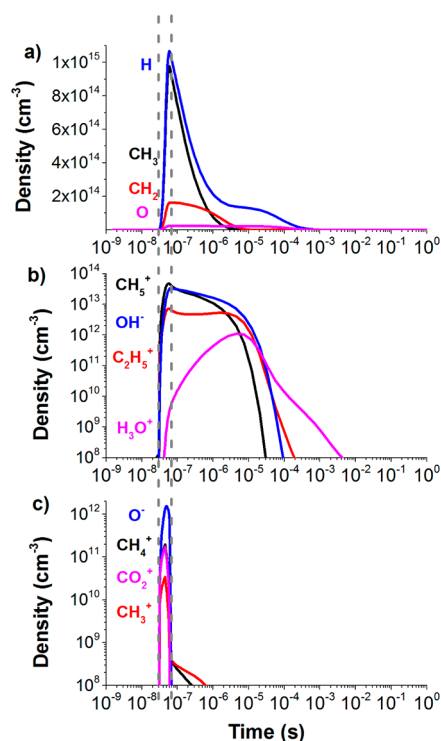


Figure 6. Calculated densities of the most important radicals (a) and ions (b,c) formed in the plasma, as a function of time during one pulse and afterglow. The gray dashed lines indicate the start and the end of the microdischarge pulse.

6(a)) reach clearly higher densities than the ions because they are more efficiently formed during the pulse (see also Figure 3 above), but their densities drop significantly in the afterglow due to recombination reactions. The most important radicals are CH_3 and H because they are both formed directly from electron impact dissociation of CH_4 . Contrary to many common assumptions (see Section 5.2 below), the OH radicals are found to play a quite minor role, with a density of 10^{10} cm^{-3} during the pulse, increasing to $4 \times 10^{11} \text{ cm}^{-3}$ during the afterglow, and then followed by a strong decline, due to the loss process $\text{CO} + \text{OH} \rightarrow \text{CO}_2 + \text{H}$.

The ions are depicted in Figure 6(b,c) and can be divided into two groups: CH_5^+ , C_2H_5^+ , H_3O^+ , and OH^- (Figure 6(b)) are formed during the pulse, but have also a considerable lifetime in the afterglow, whereas CH_4^+ , CH_3^+ , CO_2^+ , and O^- (Figure 6(c)) are only present during the pulse. The CH_5^+ , C_2H_5^+ , and OH^- ions are formed immediately, and their

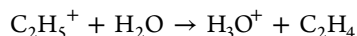
densities reach a steady state already during the pulse. This is due to a competition of formation and loss processes, i.e.,

-For CH_5^+ , there is an equilibrium between $\text{CH}_4^+ + \text{CH}_4 \rightarrow \text{CH}_5^+ + \text{CH}_3$ as the formation process and $\text{e}^- + \text{CH}_5^+ \rightarrow \text{CH}_3 + \text{H} + \text{H}$ as a loss process.

-For C_2H_5^+ , the two most important production processes (i.e., $\text{CH}_5^+ + \text{C}_2\text{H}_4 \rightarrow \text{C}_2\text{H}_5^+ + \text{CH}_4$ and $\text{CH}_3^+ + \text{CH}_4 \rightarrow \text{C}_2\text{H}_5^+ + \text{H}_2$) are in equilibrium with the two dominant loss processes (i.e., $\text{e}^- + \text{C}_2\text{H}_5^+ \rightarrow \text{C}_2\text{H}_3 + \text{H} + \text{H}$ and $\text{e}^- + \text{C}_2\text{H}_5^+ \rightarrow \text{C}_2\text{H}_2 + \text{H}_2 + \text{H}$).

-Finally, for OH^- , the dominant production processes (i.e., $\text{O}^- + \text{CH}_4 \rightarrow \text{OH}^- + \text{CH}_3$ and $\text{e}^- + \text{H}_2\text{O} \rightarrow \text{OH}^- + \text{H}$) are compensated by the loss process $\text{OH}^- + \text{CH}_3 \rightarrow \text{CH}_3\text{OH} + \text{e}^-$.

The formation of H_3O^+ ions occurs at a lower rate but continues in the afterglow because it is formed out of C_2H_5^+ ions, through



However, when all C_2H_5^+ has reacted away, the loss processes of H_3O^+ become more important than the production process, leading also to a drop in H_3O^+ density.

3.3. Reaction Path Analysis for Loss and Production of CH_4 and CO_2 . (a). Loss and Production of CH_4 . Table 2

Table 2. Overview of the Most Important Loss and Formation Reactions for CH_4 , during the Pulse and Afterglow^a

Loss processes:	
during the pulse	during the afterglow
(1) $\text{e}^- + \text{CH}_4 \rightarrow \text{CH}_3 + \text{H} + \text{e}^-$	(4) $\text{CH} + \text{CH}_4 \rightarrow \text{C}_2\text{H}_4 + \text{H}$
(2) $\text{e}^- + \text{CH}_4 \rightarrow \text{CH}_2 + \text{H}_2 + \text{e}^-$	(9) $\text{OH} + \text{CH}_4 \rightarrow \text{CH}_3 + \text{H}_2\text{O}$
(3) $\text{e}^- + \text{CH}_4 \rightarrow \text{CH} + \text{H}_2 + \text{H} + \text{e}^-$	(10) $\text{CH}_3^+ + \text{CH}_4 \rightarrow \text{C}_2\text{H}_5^+ + \text{H}_2$
(4) $\text{CH} + \text{CH}_4 \rightarrow \text{C}_2\text{H}_4 + \text{H}$	(5) $\text{CH}_4^+ + \text{CH}_4 \rightarrow \text{CH}_5^+ + \text{CH}_3$
(5) $\text{CH}_4^+ + \text{CH}_4 \rightarrow \text{CH}_5^+ + \text{CH}_3$	
(6) $\text{e}^- + \text{CH}_4 \rightarrow \text{CH}_4^+ + \text{e}^- + \text{e}^-$	
(7) $\text{O}^- + \text{CH}_4 \rightarrow \text{CH}_3 + \text{OH}^-$	
(8) $\text{CO}_2^+ + \text{CH}_4 \rightarrow \text{CH}_4^+ + \text{CO}_2$	
Formation processes:	
during the pulse	during the afterglow
(11) $\text{CH}_3 + \text{H} + \text{M} \rightarrow \text{CH}_4 + \text{M}$	(11) $\text{CH}_3 + \text{H} + \text{M} \rightarrow \text{CH}_4 + \text{M}$
	(12) $\text{CH}_5^+ + \text{C}_2\text{H}_4 \rightarrow \text{CH}_4 + \text{C}_2\text{H}_5^+$
	(13) $\text{CH}_5^+ + \text{CH}_2 \rightarrow \text{CH}_4 + \text{CH}_3^+$
	(14) $\text{CH}_5^+ + \text{H}_2\text{O} \rightarrow \text{CH}_4 + \text{H}_3\text{O}^+$

^aNote: M can be any plasma species (but typically CH_4 or CO_2 , as they have the highest densities).

lists the most important loss and formation processes for CH_4 in order of decreasing importance, during the pulse and afterglow. During the pulse, the electron impact reactions are by far the most important loss mechanisms and especially electron impact dissociation with the formation of CH_3 and H (reaction 1 of Table 2). This explains why the CH_3 and H radical densities are higher than the other radical and ion densities (see Figure 6 above). However, immediately after pulse termination, the rates of these electron impact reactions drop to nearly zero, due to the drop in electron temperature (see Figure 2 above), and in the afterglow, the chemical reactions with radicals and ions are the most important loss processes (especially reactions 4 and 9 of Table 2). Integrated over one pulse and afterglow, the electron impact reactions contribute for 77% to the loss of CH_4 , in spite of the fact that

they only occur during the pulse, while the ion and radical reactions account for 23% (see Table 3).

Table 3. Contributions of the Most Important Loss and Formation Processes for CH_4 , Integrated over the Time of One Pulse (30 ns), the Afterglow (30 ns–1s), and the Total Pulse + Afterglow

Loss processes	pulse	afterglow	pulse and afterglow
electron impact (1–3, 6)	80%	0%	77%
chemical reactions (4–5, 7–10)	20%	100%	23%
Formation processes	pulse	afterglow	pulse and afterglow
reaction 11	100%	99%	99%
reactions 12–14	0%	1%	1%

The formation processes of CH_4 are not so relevant because CH_4 is mainly lost (dissociated), but nevertheless, they are briefly discussed here, as they have a negative contribution to the conversion of CH_4 . During the pulse, the three-body recombination reaction between CH_3 and H radicals, with a gas molecule as third body (reaction 11 of Table 2), is the only production mechanism for CH_4 , and this reaction is also dominant in the afterglow. Integrated over pulse and afterglow, it contributes for 99% to the production of CH_4 (see Table 3), whereas the remaining 1% is attributed to other chemical reactions (i.e., reactions 12–14 of Table 2).

Figure 7(a,b) illustrates the absolute reaction rates of the loss and production processes, respectively, as a function of time. It

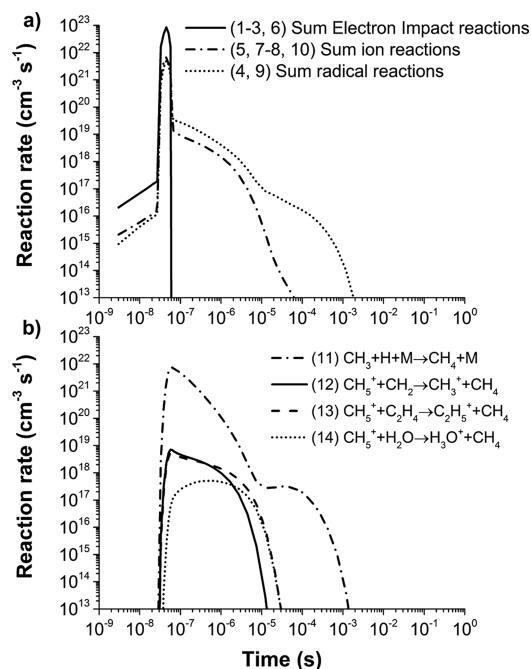


Figure 7. Rates of the most important loss (a) and formation (b) processes of CH_4 , as a function of time during one pulse and afterglow. The numbers of the reactions correspond to the numbers of Table 2.

is clear that during the pulse the rate of the electron impact reactions yielding loss of CH_4 (reactions 1–3 and 6 of Table 2) is 1 order of magnitude higher than the rate of reaction 11, which is the major production process (i.e., ca. 10^{23} vs ca. $10^{22} \text{ cm}^{-3} \text{ s}^{-1}$), so that during the pulse mainly dissociation of CH_4 takes place. In the afterglow, however, the electron impact

reactions do not play a role anymore, and the loss is mainly attributed to reactions 4–5 and 9–10, with an overall reaction rate of ca. 10^{15} – 10^{19} $\text{cm}^{-3} \text{s}^{-1}$ (see Figure 7(a)). The formation processes (reaction 11–14), on the other hand, are characterized by an overall rate of ca. 10^{18} – 10^{20} $\text{cm}^{-3} \text{s}^{-1}$ in the afterglow (see Figure 7(b)), so that the formation of CH_4 is now much larger than the loss, explaining why the CH_4 density rises again in the afterglow (see Figure 4 above).

(b). *Loss and Production of CO_2* . The most important loss and formation processes for CO_2 are listed in Table 4. During

Table 4. Overview of the Most Important Loss and Formation Reactions for CO_2 , during the Pulse and Afterglow

Loss processes:	
during the pulse	during the afterglow
(15) $\text{e}^- + \text{CO}_2 \rightarrow \text{CO} + \text{O}^-$	(18) $\text{CH}_2 + \text{CO}_2 \rightarrow \text{CH}_2\text{O} + \text{CO}$
(16) $\text{e}^- + \text{CO}_2 \rightarrow \text{CO} + \text{O} + \text{e}^-$	
(17) $\text{e}^- + \text{CO}_2 \rightarrow \text{CO}_2^+ + \text{e}^- + \text{e}^-$	
Formation processes:	
during the pulse	during the afterglow
(8) $\text{CO}_2^+ + \text{CH}_4 \rightarrow \text{CH}_4^+ + \text{CO}_2$	(19) $\text{O} + \text{CHO} \rightarrow \text{CO}_2 + \text{H}$
	(20) $\text{O} + \text{CH}_3\text{CO} \rightarrow \text{CO}_2 + \text{CH}_3$
	(21) $\text{CO} + \text{OH} \rightarrow \text{CO}_2 + \text{H}$

the pulse, the electron impact (dissociation and ionization) processes (i.e., reactions 15–17 of Table 4) are again dominant. In contrast to CH_4 , the dissociation and ionization reactions of CO_2 are equally important, which can be explained by their cross sections.⁴⁵ Note that the dissociation reactions (reactions 15–16) both produce CO, whereas only reaction 16 produces O. This explains partly why the CO density during the pulse is about a factor of 2 higher than the O density (cf. Figure 5(b) and Figure 6(a) above). Similar to CH_4 , the electron impact reaction rates drop to zero in the afterglow, and the chemical reactions with radicals become responsible for the loss of CO_2 . Especially reaction 18 of Table 4 is important, which explains the strong increase in CH_2O density in the afterglow (see Figure 5(c) above). As CO is also formed in this reaction, this explains why also the CO density increases further in the afterglow, as was clear from Figure 5(b) above. Integrated over one pulse and afterglow, the electron impact reactions (i.e., reactions 15–17) contribute for 33% to the loss of CO_2 , as is summarized in Table 5, whereas the chemical reactions with radicals contribute for 67%. This is in contrast to CH_4 , where the electron impact reactions were clearly dominant (see above).

During the pulse, the dominant formation reaction is the charge transfer between CO_2^+ and CH_4 (reaction 8 of Table 4),

Table 5. Contributions of the Most Important Loss and Formation Processes for CO_2 , Integrated over the Time of One Pulse (30 ns), the Afterglow (30 ns–1 s), and the Total Pulse + Afterglow

Loss processes	pulse	afterglow	pulse and afterglow
electron impact (15–17)	98%	0%	33%
reaction 18	2%	100%	67%
Formation processes	pulse	afterglow	pulse and afterglow
reaction 8	100%	0%	99.7%
reactions 19–21	0%	100%	0.3%

with a rate of ca. 2×10^{21} $\text{cm}^{-3} \text{s}^{-1}$. In the afterglow, this reaction becomes negligible, and some radical reactions (especially reactions 19–21 of Table 4) become important.

When looking again at the reaction rates of the different loss and formation processes as a function of time (see Figure 8(a,b)), it is obvious that during the pulse again mainly loss of

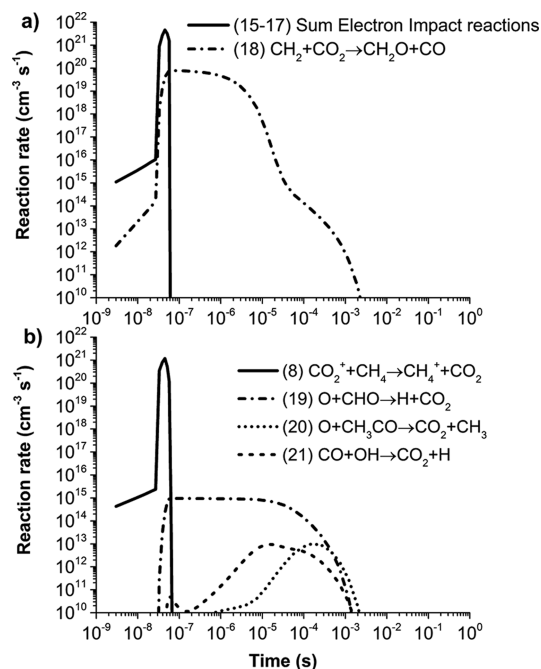


Figure 8. Rates of the most important loss (a) and formation (b) processes of CO_2 , as a function of time during one pulse and afterglow. The numbers of the reactions correspond to the numbers of Table 4.

CO_2 takes place; i.e., the total loss rate of reactions 15–17 is with a value of ca. 10^{22} $\text{cm}^{-3} \text{s}^{-1}$ nearly 1 order of magnitude higher than the rate of the most important formation process (i.e., reaction 8, ca. 3×10^{21} $\text{cm}^{-3} \text{s}^{-1}$). Nevertheless, this difference is smaller than in the case of CH_4 , which explains why the conversion of CO_2 is less pronounced during the pulse than for CH_4 (see Figure 4 above). This is an immediate consequence of the much higher binding energy of $\text{C}=\text{O}$ vs $\text{C}-\text{H}$ (i.e., 8.3 vs 4.3 eV/molecule⁴⁶), so that electron impact dissociation of CO_2 is somewhat more difficult. Furthermore, this higher stability causes the CO_2 conversion to occur predominantly by electron impact during the pulse (see Table 5), while CH_4 loss is initiated by both electrons and radicals (see Table 3), thus explaining again the higher conversion of CH_4 versus CO_2 during the discharge pulse.

In contrast to CH_4 , where the formation mechanisms became more important than the loss processes in the afterglow, for CO_2 the chemical loss processes (more specifically reaction 18) are still far more important than the formation processes (reactions 19–21), i.e., with rates of 10^{20} vs 10^{15} $\text{cm}^{-3} \text{s}^{-1}$ (see Figure 8). Hence, CO_2 will continue to be lost in the afterglow, explaining why its density drops further (see Figure 4 above).

4. FIVE CONSECUTIVE DISCHARGE PULSES: STUDY OF THE ACCUMULATION EFFECT

4.1. Power Deposition, Electron Density, and Temperature. In Figure 9, the applied power deposition and calculated electron density and temperature are plotted as a function of

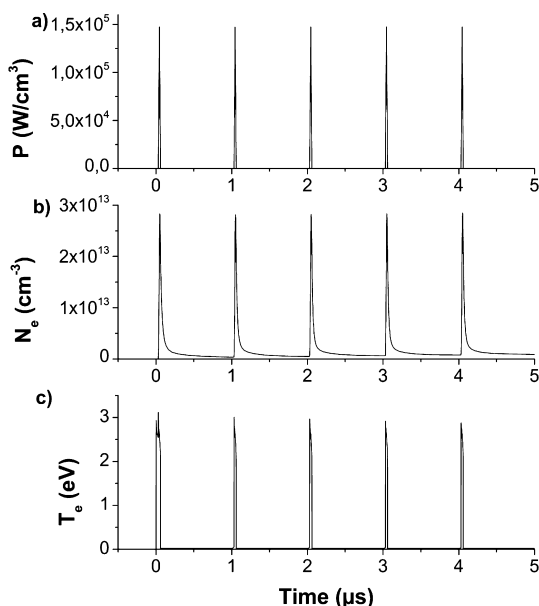


Figure 9. Applied power deposition (a) and calculated electron density (b) and electron temperature (c), as a function of time for five consecutive pulses with an interpulse period of 1 μ s.

time, for five consecutive discharge pulses, with an interpulse period of 1 μ s. This corresponds to a typical interpulse period of a filamentary DBD regime, as is observed in Figure 1 above. However, in reality, not all filaments take place at the same position; they are spatially distributed, and thus most probably not all molecules pass through all filaments. As mentioned above, in the next section, we will show results of several calculations, with different assumptions about the number of filaments per half cycle. However, as we do not know the real number of filaments that each molecule passes, we will assume a much higher pulse repetition frequency in this section compared to Section 5 for the real time-scale simulations. We use this method to find out whether some accumulation effects might occur experimentally in case some molecules would pass more pulses in a short time period because of a statistical distribution.

As is clear from Figure 9, the same triangular pulse as in a previous section, with the same power density, is applied, and therefore, the calculated electron density and temperature reach the same values as in Figure 2 above. This indicates that the plasma nearly extinguishes in the afterglow between two microdischarge pulses, even when we assume a very high pulse repetition frequency of 1 MHz.

4.2. Densities of the Plasma Species. Figure 10 illustrates the overall densities of the molecules, radicals, and positive and negative ions, as a function of time, for the five consecutive discharge pulses. In spite of the fact that the plasma nearly extinguishes between two pulses (see Figure 9 above), the consecutive pulses still lead to some accumulation of the radicals and ions, as is clear from Figure 10. Indeed, each separate pulse exhibits the same effect on the species densities, but because the formed radicals and ions do not fully recombine at a time scale of 1 μ s, i.e., the interpulse period, some accumulation in the densities is observed in Figure 10.

It appears that also the molecule density shows a slightly increasing trend. This is because the number of molecules increases during the conversion process. This can be explained

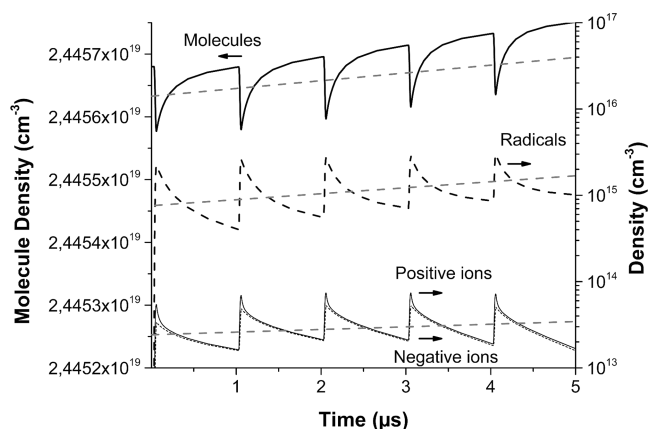


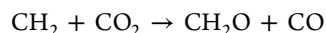
Figure 10. Calculated densities of all the molecules (left axis) and all the radicals, positive and negative ions (right axis), as a function of time for five consecutive pulses with an interpulse period of 1 μ s. The dashed lines indicate the (slightly) increasing trend of the densities as a function of time.

by reactions 2 and 18 from Tables 2 and 4, respectively, which are important loss mechanisms for CH₄ and CO₂, respectively

Reaction 2:



Reaction 18:



Hence the combination of both reactions gives: $e^- + \text{CH}_4 + \text{CO}_2 \rightarrow \text{CH}_2\text{O} + \text{CO} + \text{H}_2 + e^-$. It is indeed clear that the number of molecules in this reaction increases from two to three. However, the rise in molecule density is very minor, as appears from the left y-axis of Figure 10.

When related to the actual density values, the radical density increases by 28% per pulse, whereas the positive and negative ion densities rise by 4% and 3%, respectively, and the molecule density remains virtually constant. This indicates that, even in the case that each molecule passes through every microdischarge (filament), the accumulation effect on the molecule densities, and hence on the conversion of CH₄ and CO₂ and the selectivities of the formed products, will be very limited. On the other hand, the number of discharge pulses per half cycle will have a great influence on the electron density, and the latter will affect the calculated conversion and selectivities, as will be illustrated in Section 5.1.

The densities of the individual species are not plotted here for the five consecutive pulses, as the results are very similar as for one pulse, presented in Section 3 above, combined with the accumulation effect illustrated in Figure 10.

5. REAL TIME-SCALE SIMULATIONS

5.1. Considerations about Residence Time and Specific Energy Input. Finally, in this section, we apply the model to real time scales, corresponding to typical residence times of the gas molecules in the plasma, to obtain a first estimate of the obtained conversions, selectivities, and energy efficiency, to be compared with experimental data as a validation of the model. It should be emphasized, however, that it is not yet the focus of the present study to optimize the obtained conversions, selectivities, and energy efficiency. The latter will be elaborated in future work.

We still consider triangular microdischarge pulses of 30 ns, but with a repetition frequency of 70 kHz. This correlates to an applied frequency of 35 kHz, as used in the experiments,²⁶ assuming that each molecule passes through only one microdischarge per half cycle. The residence time for the experimental data used to validate our model is 6.8, 13.7, and 27.4 s, as calculated from the gas flow rate and the length of the reactor. This corresponds to simulating ca. 500 000–2 000 000 consecutive microdischarge pulses. Furthermore, the maximum power deposition per pulse is adapted, so that the total specific energy input (SEI) corresponds to the typical experimental values²⁶ (i.e., in the order of 18–144 J/cm³; see below).

In experiments the SEI (typically expressed in kJ/L or J/cm³) is defined as the applied power (W) divided by the gas flow rate (L/s). This is a very important quantity because it combines two of the most important experimental parameters, i.e., applied power and flow rate. Furthermore, this value can be converted into the input energy in eV per molecule, which gives us an idea about the energy cost and energy efficiency of the process under study (see below)

$$\text{SEI (eV}\cdot\text{molecule}^{-1}) = \frac{\text{power (J}\cdot\text{s}^{-1})\cdot 6.24 \times 10^{18} \text{ (eV}\cdot\text{J}^{-1})\cdot 24.5 \text{ (L}\cdot\text{mol}^{-1})}{\text{gas flow rate (L}\cdot\text{s}^{-1})\cdot 6.022 \times 10^{23} \text{ (molecule}\cdot\text{mol}^{-1})}$$

Note that the value of 24.5 L·mol⁻¹ is calculated for 298 K and 1 atm.

We performed simulations for residence times of 6.8, 13.7, and 27.4 s, exactly as used in the experiments. This corresponds to flow rates of 100, 50, and 25 mL/min, respectively, for a reactor with a plasma volume of 11.4 cm³ as used in ref 26. To obtain the same SEI as in the experiments, the maximum power deposition per discharge pulse was adapted accordingly with the different applied powers used experimentally (30, 40, 50, and 60 W) for a constant simulation microdischarge pulse frequency of 70 kHz (corresponding to the experimentally applied frequency of 35 kHz). These values of the power deposition per pulse gave again rise to calculated electron temperature values during the pulse of ~3 eV, which corresponds to typical experimental values. The resulting calculated maximum values for N_e , however, were rather on the lower limit of typical experimental values (~10¹² cm⁻³). Furthermore, the conversions were slightly overestimated. Therefore, additional simulations were performed yielding the same values of T_e but calculated values for N_e of ~10¹⁴ cm⁻³. To achieve this, the pulse frequency was lowered to 0.7 kHz, corresponding to the assumption that each molecule passes one microdischarge every 100 half cycles instead of every half cycle. This assumption does not only provide better agreement with experiment but also makes more sense intuitively, since we have spatially divided filaments, which only occupy a low volume in comparison to the total reactor volume. As will be illustrated below, these simulations still resulted in an overestimation of the conversions. However, in our calculations we assumed the same plasma power as in the experiments, whereas it is generally known that not all the plasma power goes into chemical reaction processes. Indeed, part of it is lost by reflection in the reactor and to gas heating. Furthermore, not all excitation processes of all species are taken into account, but they also “consume” part of the plasma power. Hence, we have to take these “power loss processes” into account in the simulations, by using a factor which we will call the “plasma power transfer efficiency”. That is why we performed two more

sets of simulations, assuming that only 75% and 50% of the plasma power is effectively transferred to the chemical reaction processes, while maintaining a T_e of ~3 eV and a N_e in the order of ~10¹⁴ cm⁻³. The results of all four sets of simulations will be presented in the following figures, to investigate the impact of these assumptions. It will be demonstrated that the simulations assuming N_e of ~10¹⁴ cm⁻³ with 50% plasma power transfer efficiency show the best agreement with the experiments, hence these results will be discussed in the points below.

5.2. Conversion of CH₄ and CO₂. The parameters of interest to define whether plasma technology has enough perspectives for the dry reforming of methane are, as already mentioned, the conversion of CO₂ and CH₄, the selectivity of the reaction products, and the energy cost and energy efficiency of the process. The calculated selectivity, energy cost, and energy efficiency will be presented in the next sections. Here we will present the calculated conversion and compare with experimental data. When comparing these values it is important to know how they have been defined, to avoid misinterpretation, so we will present here the definitions used in the current paper. They are adopted from ref 26, as our calculation results will be compared with the experimental data obtained in that work. The conversion of CH₄ and CO₂ is defined as

$$C_{\text{CH}_4} (\%) = \frac{\text{moles of CH}_4 \text{ converted}}{\text{moles of CH}_4 \text{ input}} \times 100$$

$$C_{\text{CO}_2} (\%) = \frac{\text{moles of CO}_2 \text{ converted}}{\text{moles of CO}_2 \text{ input}} \times 100$$

The calculated conversions of CH₄ and CO₂, as obtained with the assumption of N_e ~10¹⁴ cm⁻³ with 50% plasma power transfer efficiency (see above), are plotted in Figure 11 as a

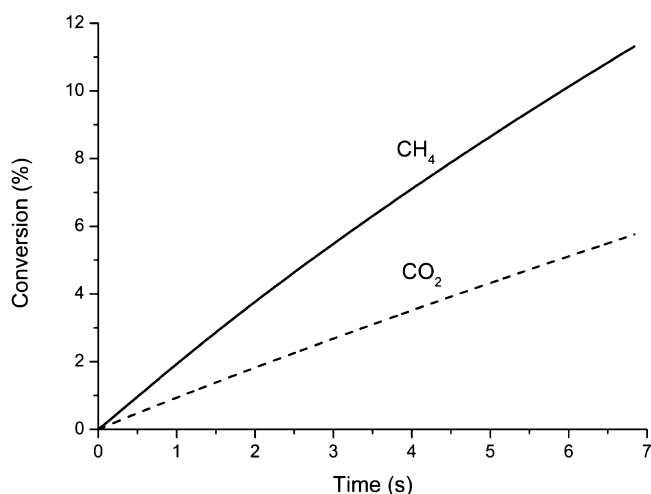


Figure 11. Calculated conversion of CH₄ and CO₂, as a function of time, for a simulated residence time of 6.84 s, with an SEI of 18 J/cm³.

function of time, for a SEI of 18 J/cm³. It is clear that the conversion of CH₄ and CO₂ increases with time, and the conversion of CH₄ is about a factor of 2 higher than the conversion of CO₂, as was anticipated from the short time-scale simulations presented in Section 3. The conversion of both gases increases more or less linearly with time, but it will saturate after a certain time, due to the competition of production and loss processes.

Figure 12 illustrates the calculated conversions of CH₄ and CO₂ as a function of discharge power (open symbols), for

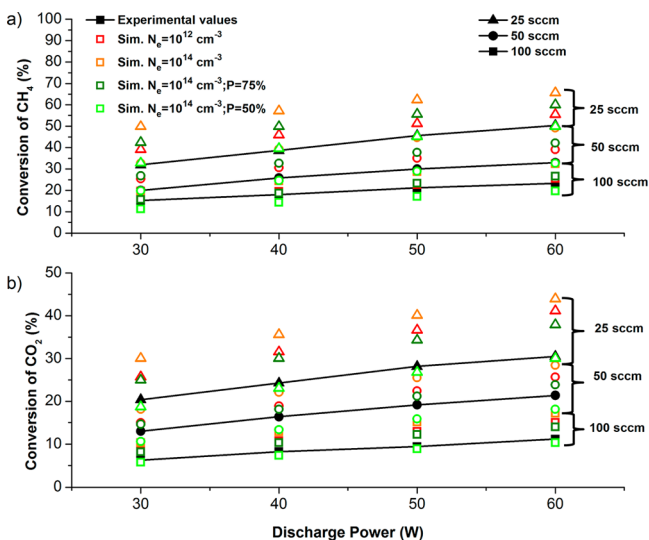


Figure 12. Comparison of the calculated (open symbols) and experimentally measured (full black symbols + trend lines) conversions of CH₄ (a) and CO₂ (b), as a function of discharge power for various flow rates (see legend).

different gas flow rates, in comparison with experimental values obtained from ref 26 (black symbols and trend lines). As explained in Section 5.1 above, four sets of simulation results are illustrated. It is clear that the results obtained with $N_e \sim 10^{12} \text{ cm}^{-3}$ and $N_e \sim 10^{14} \text{ cm}^{-3}$, assuming 100% plasma power transfer efficiency (red and orange open symbols, respectively), are systematically higher than the experimental data. The agreement is still reasonable for the data obtained with $N_e \sim 10^{12} \text{ cm}^{-3}$, but the data obtained with $N_e \sim 10^{14} \text{ cm}^{-3}$ are significantly higher. Therefore, we also performed simulations with $N_e \sim 10^{14} \text{ cm}^{-3}$, assuming a plasma power transfer efficiency of only 75% and 50% (dark and light green symbols, respectively), and this yields lower conversions, as expected. In general, the latter assumption (i.e., 50% plasma power transfer efficiency) yields an almost perfect agreement with the experimental data.

It needs to be mentioned that a relative error of 5–10% due to plasma instability should be taken into account for the experimental values obtained by GC measurement, on top of the already mentioned unknown uncertainty for the “real” experimental plasma power input. Moreover, also the calculated values are subject to some uncertainties, mainly due to uncertainties (i.e., unknown error bars) in the reaction rate coefficients, used as input in the model. Therefore, the present comparison can be considered to be fairly good for both CH₄ and CO₂ because the difference between calculated and experimental values is probably within the error bars. Moreover, all the simulations show exactly the same rising trend as the experiments. In general, this reasonable agreement between calculated and experimental conversions, in this range of power and gas flow rates, is a very important validation of the model, and it indicates that our model gives a quite realistic description of the plasma chemistry.

In Figure 13, the same data are plotted as a function of SEI, as calculated from the power values and flow rates. Again, the best agreement is reached for the simulations with $N_e \sim 10^{14}$

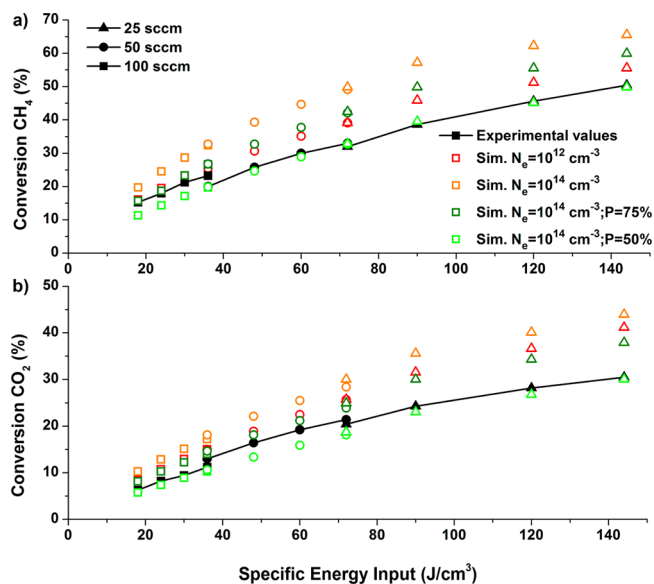


Figure 13. Calculated (open symbols) and experimentally measured (full black symbols + trend line) conversions of CH₄ (a) and CO₂ (b), as a function of SEI.

cm^{-3} , assuming 50% plasma power transfer efficiency. It is apparent from this figure that the conversion increases more or less linearly with the SEI values, which seems logical. However, a higher SEI value implies a higher energy cost, and it has therefore a negative impact on the energy efficiency (see Section 5.4 below). There will probably be an optimum between conversion, selectivity, and energy cost and efficiency, which we will investigate in future work.

Furthermore, comparing Figure 13(a,b) tells us that the CH₄ conversion is systematically higher than the CO₂ conversion, for the same SEI and residence time. This behavior was also found experimentally¹⁷ but was considered to be surprising, as for the separate gases the conversion of CO₂ is typically higher than for CH₄.¹⁶ A possible explanation, suggested in the literature,⁴⁴ is the reaction: $\text{CO} + \text{OH} \rightarrow \text{CO}_2 + \text{H}$. According to ref 47, this reaction would reduce the conversion of CO₂ in the CH₄/CO₂ mixture. However, our reaction path analysis, presented in Section 3.3 above, revealed that this reaction (i.e., reaction 21 in Table 4 above) accounts only for 0.02% of the CO₂ production, whereas reaction 8 of Table 4, i.e., $\text{CO}_2^+ + \text{CH}_4 \rightarrow \text{CH}_4^+ + \text{CO}_2$, contributes for 99% to the CO₂ production. Hence, our calculations predict that the latter reaction accounts for the reduced CO₂ conversion in the presence of CH₄. This high contribution is the result of the high reaction rate coefficient for this charge transfer process ($5.50 \times 10^{-10} \text{ cm}^3 \text{ s}^{-1}$) in combination with the high density of the second reaction species CH₄ ($1.22 \times 10^{19} \text{ cm}^{-3}$). This results in a high reaction rate ($\sim 2 \times 10^{21} \text{ cm}^{-3} \text{ s}^{-1}$) during the pulse, as is clear from Figure 8(b), where the reaction rates are plotted for the reactions that have the largest (time integrated) contribution to the formation of CO₂. This example illustrates that numerical simulations can be very useful for obtaining a better insight into the underlying physical and chemical processes, as they are based on real quantitative data (i.e., reaction rate coefficients and calculated densities). Moreover, simulations can be very useful to optimize experiments, e.g., by choosing plasma conditions which suppress reaction 8, to enhance the CO₂ conversion.

5.3. Selectivities of the Formed Products. The selectivity of the formed products is an even more important quantity than the conversion, as we target the formation of value-added chemicals or new fuels. The selectivity of H₂, CO, hydrocarbons (C_xH_y), and oxygenated hydrocarbons (C_xH_yO_z) is defined as follows²⁶

$$S_{\text{H}_2} (\%) = \frac{\text{moles of H}_2 \text{ produced}}{2 \times \text{moles of CH}_4 \text{ converted}} \times 100$$

$$S_{\text{CO}} (\%) = \frac{\text{moles of CO produced}}{\text{moles of CH}_4 \text{ converted} + \text{moles of CO}_2 \text{ converted}} \times 100$$

$$S_{\text{C}_x\text{H}_y} (\%) = \frac{x \times \text{moles of C}_x\text{H}_y \text{ produced}}{\text{moles of CH}_4 \text{ converted} + \text{moles of CO}_2 \text{ converted}} \times 100$$

$$S_{\text{C}_x\text{H}_y\text{O}_z} (\%) = \frac{x \times \text{moles of C}_x\text{H}_y\text{O}_z \text{ produced}}{\text{moles of CH}_4 \text{ converted} + \text{moles of CO}_2 \text{ converted}} \times 100$$

The calculated selectivities for the most important reaction products are plotted as a function of time in Figure 14, again for

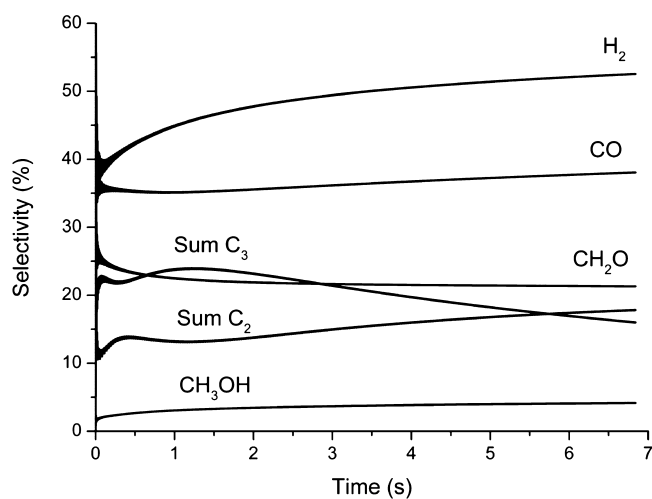


Figure 14. Calculated selectivities of the most important products, as a function of time, for a simulated residence time of 6.84 s, with an SEI of 18 J/cm³.

a fixed SEI of 18 J/cm³ and obtained with $N_e \sim 10^{14}$ cm⁻³, assuming 50% plasma power transfer efficiency. It is clear that H₂ and CO are formed with the highest selectivities, followed by the sum of C₃H₈ and C₃H₆ (noted as sum C₃), CH₂O, the sum of C₂H₆, C₂H₄, and C₂H₂ hydrocarbons (noted as sum C₂), and CH₃OH. Note that the sum of these selectivities is above 100%, which is due to the definitions given above.

It is also clear from Figure 14 that the selectivities change drastically on a very short time scale in the beginning of the simulations. This information is of interest, as it indicates that we could tune the process by varying the reaction conditions. In this respect, microplasma reactors could offer an interesting perspective, to stimulate the production of the desired components, yielding higher selectivities.

The calculated selectivities are in reasonable agreement with experimental data from the literature,^{17,26,30} as illustrated in Table 6. It needs to be mentioned that it is difficult to identify

Table 6. Calculated Selectivities of the Most Important Products and Comparison with the Experimental Data of Tu,²⁶ Gallon,¹⁷ and Wang³⁰ for an SEI of 18 J/cm³ and a 50/50 CH₄/CO₂ Ratio

	conversion		selectivity					
	CH ₄	CO ₂	H ₂	CO	sum C ₂	sum C ₃	CH ₂ O	CH ₃ OH
our simulation	16	8	55	48	6	30	13	3
Tu ²⁶	15	6	22	35	30	12	-	-
Gallon ¹⁷	10	8	23	42	18	23	-	-
Wang ³⁰	14	-	57	-	-	-	-	-

experimentally the C₂H_y product selectivities separately, and also determining the H₂ selectivity with gas chromatography is quite challenging. A more extensive validation of the obtained selectivities will be carried out in future work. Finally, it should be mentioned that the selectivities of the oxygenated products (CH₂O and CH₃OH) could not be compared, as they were not quantitatively measured. However, it is reported in the literature that they were indeed observed,^{17,31–33} which is at least some qualitative validation of our model.

The calculated and experimentally measured selectivities of the two major products, i.e., H₂ and CO, are plotted against SEI values in Figure 15. Again, the four sets of simulation results are

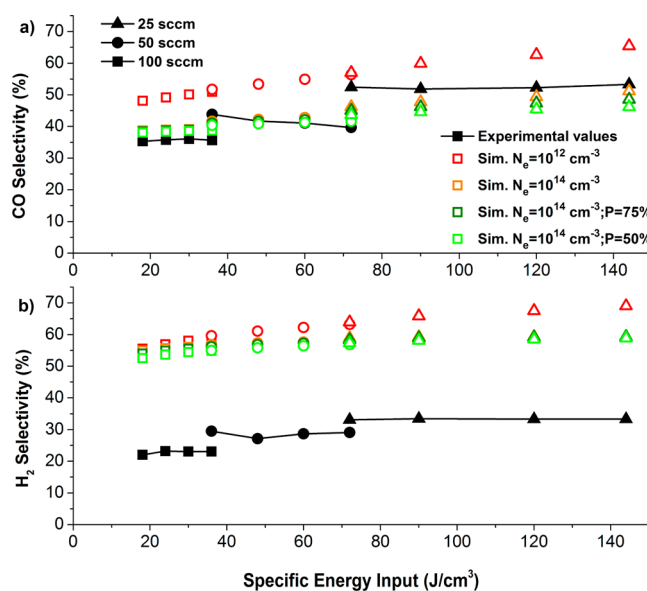


Figure 15. Calculated (open symbols) and experimentally measured (full black symbols + trend lines) selectivities of the syngas components CO (a) and H₂ (b), as a function of SEI.

illustrated. They all exhibit a rising trend with SEI. When comparing the calculated and experimental data, it appears that the calculated H₂ selectivity is overestimated by about a factor 2, while the deviations in CO selectivities are only minor and very similar to the deviation of the CO₂ conversion, presented in Figures 12 and 13 above. However, our results are in reasonable qualitative agreement with the experiments of refs 17, 26, and 30 where a similar rising trend with SEI is also observed. In the future, we will carry out a more extensive comparison with experiments to validate our modeling results. It should be stressed that our model contains a large number of chemical reactions, and by changing the reaction kinetics (e.g.,

rate coefficients) of the model, we can always obtain “a better” fit with experiments. However, we do not want to tune our rate coefficient data, simply to obtain a better agreement with experiment, without physical grounds. The present differences between calculated and measured selectivities illustrate that some chemistry, probably related to the formation or loss of H_2 , is not yet fully accounted for in the model, but at present we do not know which loss reaction would be missing or underestimated or which production reaction would be overestimated in the model. In general, we are already very satisfied with the good qualitative trends. Indeed, the focus of the present paper is rather on the detailed investigation of the plasma chemistry during one microdischarge pulse and afterglow, to mimick the filamentary behavior.

In any case, it is clear that the syngas components (H_2 and CO) are the main products formed in the dry reforming process, with a syngas ratio (H_2/CO) of ~ 1.5 . This ratio is of considerable interest for the chemical industry, as already discussed above. Also the selectivity of CH_3OH and especially CH_2O are already reasonable, and of great importance, because our simulations predict that these products can be formed directly, without the usual intermediate syngas step. In the future we will investigate how the selectivities of these two products can be increased further.

5.4. Energy Cost and Energy Efficiency of the Process.

As mentioned above, the energy cost and energy efficiency are probably the most important criteria for the dry reforming process. The thermodynamic energy cost for dry reforming is 247.3 kJ/mol (at standard conditions: 273 K) or 2.56 eV per converted molecule. The energy cost for the classical dry reforming process amounts to at least 3.42 eV/molecule, for a CH_4 conversion of 72% and a CO_2 conversion of 82%, hence corresponding to a maximum achievable energy efficiency of 58%. Therefore, this value should be the target of the plasma-based dry reforming process, to be competitive with the classical thermal process. The energy cost and energy efficiency (η) are defined here as follows

$$\begin{aligned} \text{energy cost (eV/molecule converted)} \\ &= [\text{SEI (J/cm}^3) \cdot \text{plasma volume (cm}^3)] \\ & \quad / [\text{molecules of CH}_4 \text{ converted} \\ & \quad + \text{molecules of CO}_2 \text{ converted (molecules converted)} \cdot 6.24 \\ & \quad \times 10^{18} \text{ (eV/J)}] \\ \eta (\%) &= \frac{\chi (\%) \cdot \Delta H_{298K}^0 \text{ (eV} \cdot \text{molecule}^{-1})}{\text{SEI (eV} \cdot \text{molecule}^{-1})} \\ &= \frac{\chi (\%) \cdot 2.56 \text{ (eV} \cdot \text{molecule}^{-1})}{\text{SEI (eV} \cdot \text{molecule}^{-1})} \end{aligned}$$

where χ is the conversion. In Figure 16 the calculated energy efficiency is plotted as a function of SEI for the four sets of simulations (open symbols), in comparison with the experimental data (black symbols + trend lines). It is clear that the higher conversion with increasing SEI (see Figure 13 above) does not compensate for the higher energy input with regard to the energy efficiency. Indeed, the highest energy efficiency is obtained for the lowest SEI value considered in this work, i.e., 18 J/cm³. For this condition the calculated CH_4 and CO_2 conversions were 11% and 6%, respectively, yielding an overall conversion of 8.5%. This gives rise to an energy cost of 49 eV/converted molecule and an energy efficiency of 5.2%. Note that

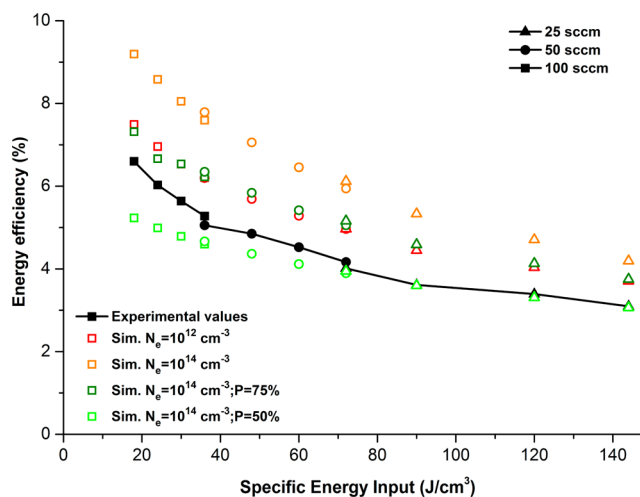


Figure 16. Calculated (open symbols) and experimentally measured (full black symbols + trend line) energy efficiency as a function of SEI.

this is still a factor of 10 lower than the classical dry reforming process. However, the latter is not unexpected, as the plasma-based dry reforming process in this paper is not yet optimized, which was indeed not the focus of the present paper. Moreover, it is well possible that a pure DBD reactor will never be competitive with the classical dry reforming. Therefore, in future work, we will also investigate the combination with catalysis, in so-called plasma catalysis, as well as the performance of other types of plasma reactors, which are stated in the literature to be more energy efficient.^{48–51}

6. CONCLUSION

The goal of this paper was to obtain a better understanding of the plasma chemistry in a DBD reactor used for the dry reforming of CH_4 and CO_2 . For this purpose, a 0D chemical kinetics model, called “Global_kin”, developed by Kushner and co-workers, was applied. The filamentary behavior of a DBD reactor was simulated by describing a large number of consecutive microdischarge pulses. We investigated in detail the plasma behavior and the reaction chemistry in one discharge pulse and its afterglow, and we made a reaction path analysis for the two gases to be converted, i.e., CH_4 and CO_2 . During the pulse, the electron impact reactions were found to be dominant, whereas chemical reactions with radicals were of primary importance in the afterglow.

We also investigated the accumulation effect of five consecutive microdischarge pulses and performed simulations for real time scales, following a large number of discharge pulses, to calculate the conversion of the gases, the selectivity of the products, and the energy cost and energy efficiency of the process. The calculated conversion for a range of different SEI values was found in good agreement with experiments, but a more extensive validation of the model, with respect to the selectivity of the formed products, needs to be carried out in future work. The main reaction products are syngas (in a H_2/CO ratio of ~ 1.5), as well as, to a lower extent, formaldehyde and methanol, which are all important for the chemical industry. Finally, the energy cost and energy efficiency of the process were calculated but were found to be not yet competitive with the existing classical dry reforming process. However, it should be mentioned that the process under study is far from optimized yet. Indeed, the main focus of the present

paper was on understanding the underlying chemical processes. A more extensive study of conversion and selectivity, and especially energy cost and energy efficiency, will be carried out in future work, among others by investigating the combination with catalysis and by the use of other types of plasma reactors.

■ ASSOCIATED CONTENT

■ Supporting Information

Table 1: Electron impact reactions with the various molecules and radicals, included in the model. Table 2: Electron–ion recombination reactions included in the model. Table 3: Neutral–neutral reactions included in the model. Table 4: Ion–neutral and ion–ion reactions included in the model. This material is available free of charge via the Internet at <http://pubs.acs.org>.

■ AUTHOR INFORMATION

Corresponding Author

*E-mail: annemie.bogaerts@ua.ac.be.

Notes

The authors declare no competing financial interest.

■ ACKNOWLEDGMENTS

This work was financially supported by the Methusalem project and the IOF-SBO project of the University of Antwerp. The calculations were carried out using the Turing HPC infrastructure at the CalcUA core facility of the Universiteit Antwerpen, a division of the Flemish Supercomputer Center VSC, funded by the Hercules Foundation, the Flemish Government (department EW1), and the Universiteit Antwerpen. Finally, we are very grateful to M. Kushner for providing the Global_kin code.

■ REFERENCES

- (1) *Sustainable Chemistry Strategic Research Agenda*; European Technology Platform for Sustainable Chemistry: Belgium, Brussels, 2005; <http://www.suschem.org/cust/documentrequest.aspx?DocID=105>.
- (2) *Fourth Assessment Report: Climate Change 2007 Synthesis Report*; Intergovernmental Panel on Climate Change IPCC: Switzerland, Geneva, 2007; http://www.ipcc.ch/publications_and_data/ar4/syr/en/contents.html.
- (3) *Sustainable Development Report Essencia*; Essencia: Belgium, Brussels, 2011; http://www.essencia.be/01/MyDocuments/SD_REPORT_ESSENSCIA_2011.pdf.
- (4) McDonough, W.; Braungart, M. *Cradle 2 Cradle: Remaking the Way We Make Things*; North Point Press: New York, 2002.
- (5) McDonough, W.; Braungart, M.; Anastas, P.; Zimmerman, J. Applying the Principles of Green Engineering to Cradle-to-Cradle Design. *Environ. Sci. Technol.* **2003**, *37* (23), 434A–441A.
- (6) Omae, I. Aspects of Carbon Dioxide Utilization. *Catal. Today* **2006**, *115* (1–4), 33–52.
- (7) De Bie, C.; Verheyde, B.; Martens, T.; Van Dijk, J.; Paulussen, S.; Bogaerts, A. Fluid Modeling of the Conversion of Methane into Higher Hydrocarbons in an Atmospheric Pressure Dielectric Barrier Discharge. *Plasma Process. Polym.* **2011**, *8*, 1033–1058.
- (8) National Energy Technology Laboratory 2010 Worldwide Gasification Database: <http://www.netl.doe.gov/technologies/coalpower/gasification/worlddatabase>.
- (9) Raju, A. S. K.; Park, C. S.; Norbeck, J. M. Synthesis Gas Production Using Steam Hydrogasification and Steam Reforming. *Fuel Process. Technol.* **2009**, *90* (2), 330–336.
- (10) Preeti, G.; Krishna, C. K.; Helen, H. L. Evaluation of the Economic and Environmental Impact of Combining Dry Reforming

With Steam Reforming of Methane. *Chem. Eng. Res. Des.* **2012**, DOI: 10.1016/j.cherd.2012.04.008.

(11) *Hydrogen fact sheet: Hydrogen production and delivery*; International Partnership for Hydrogen and Fuel Cells in the Economy: Germany, Berlin, 2005; http://www.iphe.net/docs/Fact_Sheets/Hydrogen_Production_and_Delivery.pdf.

(12) Ross, R. H. Natural Gas Reforming and CO₂ Mitigation. *Catal. Today* **2005**, *100* (1–2), 151–158.

(13) Treacy, D.; Ross, J. R. H. Carbon Dioxide Reforming of Methane Over Supported Molybdenum Carbide Catalysts. *Prepr. Pap. - Am. Chem. Soc., Div. Fuel Chem.* **2004**, *49* (2), 643–644.

(14) *HSC 4 chemistry: heat balance* Web site; <http://www.hsc-chemistry.net>.

(15) York, A. P. E.; Claridge, J. B.; Marquez-Alvarez, C.; Brungs, A. J.; Tang, S. C.; Green, M. L. H. Synthesis of Early Transition Metal Carbides and Their Application for the Reforming of Methane to Synthesis Gas. *Stud. Surf. Sci. Catal.* **1997**, *110*, 711–720.

(16) Labreque, R.; Lavoie, J.-M. Dry Reforming of Methane with CO₂ on an Electron-Activated Iron Catalytic Bed. *Bioresour. Technol.* **2011**, *102* (24), 11244–11248.

(17) Gallon, H. J. Dry Reforming of Methane Using Non-Thermal Plasma-Catalysis. *Ph.D. Dissertation*, The University of Manchester, Manchester, 2010.

(18) Petitpas, G.; Rollier, J. D.; Darmon, A.; Gonzalez-Aguilar, J.; Metkemeijer, R.; Fulcheri, L. A Comparative Study of Non-Thermal Plasma Assisted Reforming Technologies. *Int. J. Hydrogen Energy* **2007**, *32* (14), 2848–2867.

(19) Bromberg, L.; Cohn, D. R.; Rabinovich, A.; Alexeev, N. Plasma Catalytic Reforming of Methane. *Int. J. Hydrogen Energy* **1999**, *24* (12), 1131–1137.

(20) Bromberg, L.; Cohn, D. R.; Rabinovich, A.; Alexeev, N.; Samokhin, A.; Ramprasad, R.; Tamhankar, S. System Optimization and Cost Analysis of Plasma Catalytic Reforming of Natural Gas. *Int. J. Hydrogen Energy* **2000**, *25* (12), 1157–1161.

(21) Bromberg, L.; Cohn, D. R.; Rabinovich, A.; Heywood, J. Emissions Reductions Using Hydrogen From Plasmatron Fuel Converters. *Int. J. Hydrogen Energy* **2001**, *26* (10), 1115–1121.

(22) Krauss, M.; Eliasson, B.; Kogelschatz, U.; Wokaun, A. CO₂ Reforming of Methane by the Combination of Dielectric-Barrier Discharges and Catalysis. *Phys. Chem. Chem. Phys.* **2001**, *3*, 294–300.

(23) Tu, X.; Gallon, H. J.; Twigg, M. V.; Gorry, P. A.; Whitehead, J. C. Dry Reforming of Methane Over a Ni/Al₂O₃ Catalyst in a Coaxial Dielectric Barrier Discharge Reactor. *J. Phys. D: Appl. Phys.* **2011**, *44* (27), 274007.

(24) Gallon, H. J.; Tu, X.; Whitehead, J. C. Effect of Reactor Packing Materials on CO₂ Reforming of CH₄ in a Dielectric Barrier Discharge. *Plasma Process. Polym.* **2012**, *9* (1), 90–97.

(25) Gallon, H. J.; Tu, X.; Twigg, M. V.; Whitehead, J. C. Plasma-Assisted Methane Reduction of a NiO Catalyst – Low Temperature Activation of Methane and Formation of Carbon Nanofibres. *Appl. Catal. B: Environ.* **2011**, *106* (3–4), 616–620.

(26) Tu, X.; Whitehead, J. C. Plasma-Catalytic Dry Reforming of Methane in an Atmospheric Dielectric Barrier Discharge: Understanding the Synergistic Effect at Low Temperature. *Appl. Catal. B: Environ.* **2012**, *125*, 439–448.

(27) Istadi, I.; Amin, N. A. S. Modelling and Optimization of Catalytic–Dielectric Barrier Discharge Plasma Reactor for Methane and Carbon Dioxide Conversion Using Hybrid Artificial Neural Network—Genetic Algorithm Technique. *Chem. Eng. Sci.* **2007**, *62* (23), 6568–6581.

(28) Zou, J. J.; Zhang, Y.; Liu, C. J.; Li, Y.; Eliasson, B. Starch-Enhanced Synthesis of Oxygenates from Methane and Carbon Dioxide Using Dielectric-Barrier Discharges. *Plasma Chem. Plasma Process.* **2003**, *23* (1), 69–82.

(29) Liu, C. J.; Xu, G. H.; Wang, T. Non-Thermal Plasma Approaches in CO₂ Utilization. *Fuel Process. Technol.* **1999**, *58* (2–3), 119–134.

- (30) Wang, Q.; Yan, B.-H.; Yin, Y.; Cheng, Y. Investigation of Dry reforming of Methane in a Dielectric Barrier Discharge Reactor. *Plasma Chem. Plasma Process.* **2009**, *29* (3), 217–228.
- (31) Liu, C. J.; Xue, B.; Eliasson, B.; He, F.; Li, Y.; Xu, G.-H. Methane Conversion to Higher Hydrocarbons in the Presence of Carbon Dioxide Using Dielectric-Barrier Discharge Plasmas. *Plasma Chem. Plasma Process.* **2001**, *21* (3), 301–310.
- (32) Liu, C. J.; Li, Y.; Zhang, Y. P.; Wang, Y.; Zou, J.; Eliasson, B.; Xue, B. Production of Acetic Acid Directly from Methane and Carbon Dioxide Using Dielectric-Barrier Discharges. *Chem. Lett.* **2001**, *12*, 1304–1305.
- (33) Nair, S. A.; Nozaki, T.; Okazaki, K. Methane Oxidative Conversion Pathways in a Dielectric Barrier Discharge Reactor - Investigation of Gas Phase Mechanism. *Chem. Eng. J.* **2007**, *132* (1–3), 85–95.
- (34) Kraus, M.; Egli, W.; Haffner, K.; Eliasson, B.; Kogelschatz, U.; Wokaun, A. Investigation of Mechanistic Aspects of the Catalytic CO₂ Reforming of Methane in a Dielectric-Barrier Discharge Using Optical Emission Spectroscopy and Kinetic Modeling. *Phys. Chem. Chem. Phys.* **2002**, *4* (4), 668–675.
- (35) Kroker, T.; Kolb, T.; Schenk, A.; Krawczyk, K.; Mlotek, M.; Gericke, K.-H. Catalytic Conversion of Simulated Biogas Mixtures to Synthesis Gas in a Fluidized Bed Reactor Supported by a DBD. *Plasma Chem. Plasma Process.* **2012**, *32*, 565–582.
- (36) Scarduelli, G.; Guella, G.; Ascenzi, D.; Tosi, P. Synthesis of Liquid Organic Compounds from CH₄ and CO₂ in a Dielectric Barrier Discharge Operating at Atmospheric Pressure. *Plasma Process. Polym.* **2011**, *8*, 25–31.
- (37) Goujard, V.; Tatiboue, J.-M.; Batiot-Dupeyrat, C. Carbon Dioxide Reforming of Methane Using a Dielectric Barrier Discharge Reactor: Effect of Helium Dilution and Kinetic Model. *Plasma Chem. Plasma Process.* **2011**, *31*, 315–325.
- (38) Dorai, R.; Hassouni, K.; Kushner, M. J. Consequences of Propene and Propane on Plasma Remediation of NO_x. *J. Appl. Phys.* **2000**, *88* (10), 6060–6071.
- (39) Dorai, R. Modeling of Atmospheric Pressure Plasma Processing of Gasses and Surfaces. *Ph.D. Dissertation*, University of Illinois, Champaign, IL, 2002.
- (40) De Bie, C., paper in preparation.
- (41) Kogelschatz, U. Dielectric-Barrier Discharges: Their History, Discharge Physics, and Industrial Applications. *Plasma Chem. Plasma Process.* **2003**, *23* (1), 146.
- (42) Fridman, A. *Plasma Chemistry*; Cambridge University Press: Cambridge, 2008.
- (43) Preeti, G.; Krishna, C. K.; Helen, H. L. Evaluation of the Economic and Environmental Impact of Combining Dry Reforming with Steam Reforming of Methane. *Chem. Eng. Res. Des.* **2012**, DOI: 10.1016/j.cherd.2012.04.008.
- (44) De Bie, C.; Martens, T.; Van Dijk, J.; Paulussen, S.; Verheyde, B.; Corthals, S.; Bogaerts, A. Dielectric Barrier Discharges Used for the Conversion of Greenhouse Gases: Modeling the Plasma Chemistry by Fluid Simulations. *Plasma Sources Sci. Technol.* **2011**, *20*, 024008.
- (45) Itikawa, Y. Cross Sections for Electron Collisions With Carbon Dioxide. *J. Phys. Chem. Ref. Data* **2002**, *31*, 749–767.
- (46) *National Standard Reference Data Series*, No. 31; National Bureau of Standards: Washington, DC, 1970.
- (47) Yao, S. L.; Okumoto, M.; Nakayama, A.; Suzuki, E. Plasma Reforming and Coupling of Methane with Carbon Dioxide. *Energy Fuels* **2001**, *15* (5), 1295–1299.
- (48) Gutsol, A.; Rabinovich, A.; Fridman, A. Combustion-Assisted Plasma in Fuel Conversion. *J. Phys. D: Appl. Phys.* **2011**, DOI: 10.1088/0022-3727/44/27/274001.
- (49) Bo, Z.; Yan, J.; Li, X.; Chi, Y.; Cen, K. Plasma Assisted Dry Methane Reforming Using Gliding Arc Gas Discharge: Effect of Feed Gases Proportion. *Int. J. Hydrogen Energy* **2009**, *33* (20), 5545–5553.
- (50) Fidalgo, B.; Dominguez, A.; Pis, J. J.; Menéndez, J. A. Microwave-Assisted Dry Reforming of Methane. *Int. J. Hydrogen Energy* **2008**, *33* (16), 4337–4344.
- (51) Zhang, J. Q.; Yang, Y. J.; Zhang, J. S.; Liu, Q. Study on the Conversion of CH₄ and CO₂ Using a Pulsed Microwave Plasma Under Atmospheric Pressure. *Acta Chim. Sin.* **2002**, *60* (11), 1973–1980.

Plasma-Based Dry Reforming: A Computational Study Ranging from Nanoseconds to Seconds Timescale

*Ramses Snoeckx¹, Robby Aerts¹, Xin Tu² and Annemie Bogaerts^{*1}*

¹Research group PLASMANT, University of Antwerp, Department of Chemistry

Universiteitsplein 1, B-2610 Wilrijk-Antwerp, Belgium

² Department of Electrical Engineering and Electronics, University of Liverpool, Liverpool L69

3GJ, United Kingdom

Overview of the reactions included in the model.

Table 1: Electron impact reactions with the various molecules and radicals, included in the model. These reactions are treated by energy-dependent cross sections, and the references where these cross sections were adopted from, are also included. For the vibrational and electronic excitations, several individual excitations are included, as indicated by the number between brackets.

Momentum Transfer	$e^- + CH_4$	$\rightarrow e^- + CH_4$		1
Vibrational Excitation	$e^- + CH_4$	$\rightarrow e^- + CH_4^*$	(2)	1
Ionization	$e^- + CH_4$	$\rightarrow 2e^- + CH_4^+$		2
Dissociative Ionization	$e^- + CH_4$	$\rightarrow 2e^- + CH_3^+ + H$		2
	$e^- + CH_4$	$\rightarrow 2e^- + CH_2^+ + H_2$		2
Dissociation	$e^- + CH_4$	$\rightarrow e^- + CH_3 + H$		3,4
	$e^- + CH_4$	$\rightarrow e^- + CH_2 + H_2$		3,4
	$e^- + CH_4$	$\rightarrow e^- + CH + H_2 + H$		3,4
	$e^- + CH_4$	$\rightarrow e^- + C + 2H_2$		3,4
Ionization	$e^- + CH_3$	$\rightarrow 2e^- + CH_3^+$		2
Dissociative Ionization	$e^- + CH_3$	$\rightarrow 2e^- + CH_2^+ + H$		2
	$e^- + CH_3$	$\rightarrow 2e^- + CH^+ + H_2$		2
Dissociation	$e^- + CH_3$	$\rightarrow e^- + CH_2 + H$		3,4
	$e^- + CH_3$	$\rightarrow e^- + CH + H_2$		3,4
Ionization	$e^- + CH_2$	$\rightarrow 2e^- + CH_2^+$		2
Dissociation	$e^- + CH_2$	$\rightarrow e^- + CH + H$		3,4
Ionization	$e^- + CH$	$\rightarrow 2e^- + CH^+$		2
Dissociation	$e^- + CH$	$\rightarrow e^- + C + H$		3,4
Momentum Transfer	$e^- + C_2H_6$	$\rightarrow e^- + C_2H_6$		1
Vibrational Excitation	$e^- + C_2H_6$	$\rightarrow e^- + C_2H_6^*$	(3)	1
Ionization	$e^- + C_2H_6$	$\rightarrow 2e^- + C_2H_6^+$		2
Dissociative Ionization	$e^- + C_2H_6$	$\rightarrow 2e^- + C_2H_5^+ + H$		2
	$e^- + C_2H_6$	$\rightarrow 2e^- + C_2H_4^+ + H_2$		2
	$e^- + C_2H_6$	$\rightarrow 2e^- + C_2H_3^+ + H_2 + H$		2
	$e^- + C_2H_6$	$\rightarrow 2e^- + C_2H_2^+ + 2H_2$		2
	$e^- + C_2H_6$	$\rightarrow 2e^- + CH_3^+ + CH_3$		2
Dissociation	$e^- + C_2H_6$	$\rightarrow e^- + C_2H_5 + H$		5,6
	$e^- + C_2H_6$	$\rightarrow e^- + C_2H_4 + H_2$		5,6
Ionization	$e^- + C_2H_5$	$\rightarrow 2e^- + C_2H_5^+$		2
Dissociative Ionization	$e^- + C_2H_5$	$\rightarrow 2e^- + C_2H_4^+ + H$		2
	$e^- + C_2H_5$	$\rightarrow 2e^- + C_2H_3^+ + H_2$		2

	$e^- + C_2H_5$	\rightarrow	$2e^- + C_2H_2^+ + H_2 + H$	2
Dissociation	$e^- + C_2H_5$	\rightarrow	$e^- + C_2H_4 + H$	5,6
	$e^- + C_2H_5$	\rightarrow	$e^- + C_2H_3 + H_2$	5,6
Momentum Transfer	$e^- + C_2H_4$	\rightarrow	$e^- + C_2H_4$	1
Vibrational Excitation	$e^- + C_2H_4$	\rightarrow	$e^- + C_2H_4^*$	(2) 1
Ionization	$e^- + C_2H_4$	\rightarrow	$2e^- + C_2H_4^+$	2
Dissociative Ionization	$e^- + C_2H_4$	\rightarrow	$2e^- + C_2H_3^+ + H$	2
	$e^- + C_2H_4$	\rightarrow	$2e^- + C_2H_2^+ + H_2$	2
Dissociation	$e^- + C_2H_4$	\rightarrow	$e^- + C_2H_3 + H$	5,6
	$e^- + C_2H_4$	\rightarrow	$e^- + C_2H_2 + H_2$	5,6
Ionization	$e^- + C_2H_3$	\rightarrow	$2e^- + C_2H_3^+$	2
Dissociative Ionization	$e^- + C_2H_3$	\rightarrow	$2e^- + C_2H_2^+ + H$	2
Dissociation	$e^- + C_2H_3$	\rightarrow	$e^- + C_2H_2 + H$	5,6
	$e^- + C_2H_3$	\rightarrow	$e^- + C_2H + H_2$	5,6
Momentum Transfer	$e^- + C_2H_2$	\rightarrow	$e^- + C_2H_2$	1
Vibrational Excitation	$e^- + C_2H_2$	\rightarrow	$e^- + C_2H_2^*$	(3) 1
Ionization	$e^- + C_2H_2$	\rightarrow	$2e^- + C_2H_2^+$	2
Dissociation	$e^- + C_2H_2$	\rightarrow	$e^- + C_2H + H$	5,6
Dissociation	$e^- + C_2H$	\rightarrow	$e^- + C + CH$	5,6
Momentum Transfer	$e^- + C_3H_8$	\rightarrow	$e^- + C_3H_8$	1
Vibrational Excitation	$e^- + C_3H_8$	\rightarrow	$e^- + C_3H_8^*$	(2) 1
Dissociative Ionization	$e^- + C_3H_8$	\rightarrow	$2e^- + C_2H_5^+ + CH_3$	2
	$e^- + C_3H_8$	\rightarrow	$2e^- + C_2H_4^+ + CH_4$	2
Dissociation	$e^- + C_3H_8$	\rightarrow	$e^- + C_3H_7 + H$	5,6
	$e^- + C_3H_8$	\rightarrow	$e^- + C_3H_6 + H_2$	5,6
	$e^- + C_3H_8$	\rightarrow	$e^- + C_2H_4 + CH_4$	5,6
Dissociative Ionization	$e^- + C_3H_7$	\rightarrow	$2e^- + C_2H_5^+ + CH_2$	5,6
	$e^- + C_3H_7$	\rightarrow	$2e^- + C_2H_4^+ + CH_3$	5,6
	$e^- + C_3H_7$	\rightarrow	$2e^- + C_2H_3^+ + CH_4$	5,6
	$e^- + C_3H_7$	\rightarrow	$2e^- + CH_3^+ + C_2H_4$	5,6
Dissociation	$e^- + C_3H_7$	\rightarrow	$e^- + C_3H_6 + H$	5,6

	$e^- + C_3H_7$	$\rightarrow e^- + C_2H_4 + CH_3$		5, 6
	$e^- + C_3H_7$	$\rightarrow e^- + C_2H_3 + CH_4$		5, 6
Dissociative Ionization	$e^- + C_3H_6$	$\rightarrow 2e^- + C_2H_5^+ + CH$		5, 6
	$e^- + C_3H_6$	$\rightarrow 2e^- + C_2H_4^+ + CH_2$		5, 6
	$e^- + C_3H_6$	$\rightarrow 2e^- + C_2H_3^+ + CH_3$		5, 6
	$e^- + C_3H_6$	$\rightarrow 2e^- + C_2H_2^+ + CH_4$		5, 6
	$e^- + C_3H_6$	$\rightarrow 2e^- + CH_3^+ + C_2H_3$		5, 6
Dissociation	$e^- + C_3H_6$	$\rightarrow e^- + C_2H_2 + CH_4$		5, 6
Momentum Transfer	$e^- + H_2$	$\rightarrow e^- + H_2$		7
Vibrational Excitation	$e^- + H_2$	$\rightarrow e^- + H_2^*$	(3)	8
Dissociation	$e^- + H_2$	$\rightarrow e^- + 2H$		9
Momentum Transfer	$e^- + O_2$	$\rightarrow e^- + O_2$		10
Ionization	$e^- + O_2$	$\rightarrow 2e^- + O_2^+$		11
Dissociative Attachment	$e^- + O_2$	$\rightarrow O^- + O$		10
Dissociation	$e^- + O_2$	$\rightarrow e^- + 2O$	(2)	10
Momentum Transfer	$e^- + O$	$\rightarrow e^- + O$		12
Electronic Excitation	$e^- + O$	$\rightarrow e^- + O^*$	(2)	13
Attachment	$e^- + O + O_2$	$\rightarrow O^- + O_2$		10
Momentum Transfer	$e^- + CO_2$	$\rightarrow e^- + CO_2$		14
Vibrational Excitation	$e^- + CO_2$	$\rightarrow e^- + CO_2^*$	(3)	14
Electronic Excitation	$e^- + CO_2$	$\rightarrow e^- + CO_2^*$	(2)	15
Ionization	$e^- + CO_2$	$\rightarrow 2e^- + CO_2^+$		14
Dissociative Attachment	$e^- + CO_2$	$\rightarrow O^- + CO$		14
Dissociation	$e^- + CO_2$	$\rightarrow e^- + CO + O$		14
Momentum Transfer	$e^- + CO$	$\rightarrow e^- + CO$		8
Vibrational Excitation	$e^- + CO$	$\rightarrow e^- + CO^*$	(1)	8
Electronic Excitation	$e^- + CO$	$\rightarrow e^- + CO^*$	(5)	15
Dissociative Attachment	$e^- + CO$	$\rightarrow O^- + C$		16
Dissociation	$e^- + CO$	$\rightarrow e^- + C + O$		17
Momentum Transfer	$e^- + H_2O$	$\rightarrow e^- + H_2O$		18
Vibrational Excitation	$e^- + H_2O$	$\rightarrow e^- + H_2O^*$	(2)	18

Dissociative Attachment	$e^- + H_2O$	$\rightarrow O^- + H_2$	18
	$e^- + H_2O$	$\rightarrow OH^- + H$	18
Dissociation	$e^- + H_2O$	$\rightarrow e^- + OH + H$	18
	$e^- + H_2O$	$\rightarrow e^- + O + H_2$	18
Dissociation	$e^- + OH$	$\rightarrow e^- + O + H$	19

Table 2: Electron-ion recombination reactions included in the model, as well as the corresponding rate coefficients for 300 K and the references where these data were adopted from.

e^-	+	CH_5^+	\rightarrow	CH_3	+	$2H$	2.57×10^{-07}	$cm^3 s^{-1}$	3, 20
e^-	+	CH_5^+	\rightarrow	CH_2	+	$H_2 + H$	6.10×10^{-08}	$cm^3 s^{-1}$	3, 20
e^-	+	CH_4^+	\rightarrow	CH_3	+	H	1.18×10^{-08}	$cm^3 s^{-1}$	3, 20
e^-	+	CH_4^+	\rightarrow	CH_2	+	$2H$	2.42×10^{-08}	$cm^3 s^{-1}$	3, 20
e^-	+	CH_4^+	\rightarrow	CH	+	$H_2 + H$	1.41×10^{-08}	$cm^3 s^{-1}$	3, 20
e^-	+	CH_3^+	\rightarrow	CH_2	+	H	2.25×10^{-08}	$cm^3 s^{-1}$	3, 20
e^-	+	CH_3^+	\rightarrow	CH	+	H_2	7.88×10^{-09}	$cm^3 s^{-1}$	3, 20
e^-	+	CH_3^+	\rightarrow	CH	+	$2H$	9.00×10^{-09}	$cm^3 s^{-1}$	3, 20
e^-	+	CH_3^+	\rightarrow	C	+	$H_2 + H$	1.69×10^{-08}	$cm^3 s^{-1}$	3, 20
e^-	+	CH_2^+	\rightarrow	CH	+	H	1.00×10^{-08}	$cm^3 s^{-1}$	3, 20
e^-	+	CH_2^+	\rightarrow	C	+	H_2	4.82×10^{-09}	$cm^3 s^{-1}$	3, 20
e^-	+	CH_2^+	\rightarrow	C	+	$2H$	2.53×10^{-08}	$cm^3 s^{-1}$	3, 20
e^-	+	CH^+	\rightarrow	C	+	H	3.23×10^{-08}	$cm^3 s^{-1}$	3, 20
e^-	+	$C_2H_6^+$	\rightarrow	C_2H_5	+	H	2.19×10^{-08}	$cm^3 s^{-1}$	6
e^-	+	$C_2H_6^+$	\rightarrow	C_2H_4	+	$2H$	3.36×10^{-08}	$cm^3 s^{-1}$	6
e^-	+	$C_2H_5^+$	\rightarrow	C_2H_4	+	H	7.70×10^{-09}	$cm^3 s^{-1}$	6
e^-	+	$C_2H_5^+$	\rightarrow	C_2H_3	+	$2H$	1.92×10^{-08}	$cm^3 s^{-1}$	6
e^-	+	$C_2H_5^+$	\rightarrow	C_2H_2	+	$H_2 + H$	1.9×10^{-08}	$cm^3 s^{-1}$	6
e^-	+	$C_2H_5^+$	\rightarrow	C_2H_2	+	$3H$	8.98×10^{-09}	$cm^3 s^{-1}$	6
e^-	+	$C_2H_5^+$	\rightarrow	CH_3	+	CH_2	9.62×10^{-09}	$cm^3 s^{-1}$	6
e^-	+	$C_2H_4^+$	\rightarrow	C_2H_3	+	H	8.29×10^{-09}	$cm^3 s^{-1}$	6
e^-	+	$C_2H_4^+$	\rightarrow	C_2H_2	+	$2H$	3.43×10^{-08}	$cm^3 s^{-1}$	6
e^-	+	$C_2H_4^+$	\rightarrow	C_2H	+	$H_2 + H$	5.53×10^{-09}	$cm^3 s^{-1}$	6
e^-	+	$C_2H_3^+$	\rightarrow	C_2H_2	+	H	1.34×10^{-08}	$cm^3 s^{-1}$	6

e^-	+	$C_2H_3^+$	\rightarrow	C_2H	+	$2H$	2.74×10^{-08}	$cm^3 s^{-1}$	⁶
e^-	+	$C_2H_2^+$	\rightarrow	C_2H	+	H	1.87×10^{-08}	$cm^3 s^{-1}$	⁶
e^-	+	$C_2H_2^+$	\rightarrow	$2CH$			4.87×10^{-09}	$cm^3 s^{-1}$	⁶
e^-	+	O_2^+	\rightarrow	O	+	O	1.94×10^{-20}	$cm^3 s^{-1}$	²¹
e^-	+	$O_2^+ + O_2$	\rightarrow	O_2	+	O_2	1.00×10^{-26}	$cm^3 s^{-1}$	²¹
e^-	+	CO_2^+	\rightarrow	CO	+	O	2.71×10^{-07}	$cm^3 s^{-1}$	²⁰
e^-	+	H_3O^+	\rightarrow	H_2O	+	H	2.45×10^{-08}	$cm^3 s^{-1}$	²⁰
e^-	+	H_3O^+	\rightarrow	OH	+	H_2	6.58×10^{-09}	$cm^3 s^{-1}$	²⁰
e^-	+	H_3O^+	\rightarrow	OH	+	$2H$	4.02×10^{-09}	$cm^3 s^{-1}$	²⁰

Table 3: Neutral-neutral reactions included in the model, as well as the corresponding rate coefficients for 300 K and the references where these data were adopted from. Note a means that this value is an estimated value; note b means that the rate coefficient is adjusted in the model for a three-body collision by dividing by $2.446 \times 10^{19} \text{ cm}^{-3}$, i.e., the density of the background gas.

CH ₄	+	CH ₂	→	CH ₃	+	CH ₃	$3.01 \times 10^{-19} \text{ cm}^3 \text{ s}^{-1}$	22		
CH ₄	+	CH	→	C ₂ H ₄	+	H	$9.74 \times 10^{-11} \text{ cm}^3 \text{ s}^{-1}$	23		
CH ₄	+	C ₂ H ₅	→	C ₂ H ₆	+	CH ₃	$1.83 \times 10^{-24} \text{ cm}^3 \text{ s}^{-1}$	22		
CH ₄	+	C ₂ H ₃	→	C ₂ H ₄	+	CH ₃	$2.28 \times 10^{-18} \text{ cm}^3 \text{ s}^{-1}$	22		
CH ₄	+	C ₂ H	→	C ₂ H ₂	+	CH ₃	$1.31 \times 10^{-12} \text{ cm}^3 \text{ s}^{-1}$	22		
CH ₄	+	C ₃ H ₇	→	C ₃ H ₈	+	CH ₃	$4.38 \times 10^{-24} \text{ cm}^3 \text{ s}^{-1}$	24		
CH ₄	+	H	→	CH ₃	+	H ₂	$8.43 \times 10^{-19} \text{ cm}^3 \text{ s}^{-1}$	23		
CH ₃	+	CH ₃	→	C ₂ H ₅	+	H	$2.71 \times 10^{-19} \text{ cm}^3 \text{ s}^{-1}$	25		
CH ₃	+	CH ₃	+	M	→	C ₂ H ₆	+	M	$1.56 \times 10^{-26} \text{ cm}^6 \text{ s}^{-1}$	23
CH ₃	+	CH ₂	→	C ₂ H ₄	+	H	$7.01 \times 10^{-11} \text{ cm}^3 \text{ s}^{-1}$	23		
CH ₃	+	C ₂ H ₆	→	C ₂ H ₅	+	CH ₄	$7.21 \times 10^{-21} \text{ cm}^3 \text{ s}^{-1}$	23		
CH ₃	+	C ₂ H ₅	→	C ₂ H ₄	+	CH ₄	$1.91 \times 10^{-12} \text{ cm}^3 \text{ s}^{-1}$	23		
CH ₃	+	C ₂ H ₅	+	M	→	C ₃ H ₈	+	M	$1.00 \times 10^{-28} \text{ cm}^6 \text{ s}^{-1}$	a
CH ₃	+	C ₂ H ₄	→	C ₂ H ₃	+	CH ₄	$1.94 \times 10^{-21} \text{ cm}^3 \text{ s}^{-1}$	22		
CH ₃	+	C ₂ H ₃	→	C ₂ H ₂	+	CH ₄	$6.51 \times 10^{-13} \text{ cm}^3 \text{ s}^{-1}$	22		
CH ₃	+	C ₂ H ₃	+	M	→	C ₃ H ₆	+	M	$1.20 \times 10^{-10} \text{ cm}^3 \text{ s}^{-1}$	26
CH ₃	+	C ₂ H ₃	+	M	→	C ₃ H ₆	+	M	$4.91 \times 10^{-30} \text{ cm}^6 \text{ s}^{-1}$	b
CH ₃	+	C ₂ H ₂	→	CH ₄	+	C ₂ H	$7.65 \times 10^{-26} \text{ cm}^3 \text{ s}^{-1}$	22		
CH ₃	+	C ₃ H ₈	→	C ₃ H ₇	+	CH ₄	$1.02 \times 10^{-20} \text{ cm}^3 \text{ s}^{-1}$	24		
CH ₃	+	C ₃ H ₇	→	C ₃ H ₆	+	CH ₄	$3.07 \times 10^{-12} \text{ cm}^3 \text{ s}^{-1}$	24		
CH ₃	+	H ₂	→	CH ₄	+	H	$9.9 \times 10^{-21} \text{ cm}^3 \text{ s}^{-1}$	23		
CH ₃	+	H	→	CH ₂	+	H ₂	$9.96 \times 10^{-22} \text{ cm}^3 \text{ s}^{-1}$	23		
CH ₃	+	H	+	M	→	CH ₄	+	M	$2.97 \times 10^{-28} \text{ cm}^6 \text{ s}^{-1}$	23

CH ₂	+	CH ₂	→	C ₂ H ₂	+	2H	5.27 x 10 ⁻¹¹	cm ³ s ⁻¹	23		
CH ₂	+	C ₂ H ₅	→	C ₂ H ₄	+	CH ₃	3.01 x 10 ⁻¹¹	cm ³ s ⁻¹	22		
CH ₂	+	C ₂ H ₃	→	C ₂ H ₂	+	CH ₃	3.01 x 10 ⁻¹¹	cm ³ s ⁻¹	22		
CH ₂	+	C ₂ H	→	C ₂ H ₂	+	CH	3.01 x 10 ⁻¹¹	cm ³ s ⁻¹	22		
CH ₂	+	C ₃ H ₈	→	C ₃ H ₇	+	CH ₃	1.02 x 10 ⁻²⁰	cm ³ s ⁻¹	24		
CH ₂	+	C ₃ H ₇	→	C ₂ H ₄	+	C ₂ H ₅	3.01 x 10 ⁻¹¹	cm ³ s ⁻¹	24		
CH ₂	+	C ₃ H ₇	→	C ₃ H ₆	+	CH ₃	3.01 x 10 ⁻¹²	cm ³ s ⁻¹	24		
CH ₂	+	H ₂	→	CH ₃	+	H	5.00 x 10 ⁻¹⁵	cm ³ s ⁻¹	22		
CH ₂	+	H	→	CH	+	H ₂	2.01 x 10 ⁻¹⁰	cm ³ s ⁻¹	23		
CH	+	C ₂ H ₆	+	M	→	C ₃ H ₇	+	M	2.78 x 10 ⁻¹⁰	cm ³ s ⁻¹	23
CH	+	C ₂ H ₆	+	M	→	C ₃ H ₇	+	M	1.14 x 10 ⁻²⁹	cm ⁶ s ⁻¹	^b
CH	+	H ₂	→	CH ₂	+	H	6.80 x 10 ⁻¹³	cm ³ s ⁻¹	23		
CH	+	H	→	C	+	H ₂	1.00 x 10 ⁻¹⁰	cm ³ s ⁻¹	27		
C	+	H ₂	→	CH	+	H	1.50 x 10 ⁻¹⁰	cm ³ s ⁻¹	28		
C ₂ H ₆	+	C ₂ H ₃	→	C ₂ H ₅	+	C ₂ H ₄	3.39 x 10 ⁻²¹	cm ³ s ⁻¹	22		
C ₂ H ₆	+	C ₂ H	→	C ₂ H ₂	+	C ₂ H ₅	5.99 x 10 ⁻¹²	cm ³ s ⁻¹	22		
C ₂ H ₆	+	C ₃ H ₇	→	C ₃ H ₈	+	C ₂ H ₅	3.16 x 10 ⁻²²	cm ³ s ⁻¹	24		
C ₂ H ₆	+	H	→	C ₂ H ₅	+	H ₂	4.96 x 10 ⁻¹⁷	cm ³ s ⁻¹	23		
C ₂ H ₅	+	C ₂ H ₅	→	C ₂ H ₆	+	C ₂ H ₄	2.41 x 10 ⁻¹²	cm ³ s ⁻¹	23		
C ₂ H ₅	+	C ₂ H	→	C ₂ H ₄	+	C ₂ H ₂	3.01 x 10 ⁻¹²	cm ³ s ⁻¹	22		
C ₂ H ₅	+	C ₃ H ₈	→	C ₂ H ₆	+	C ₃ H ₇	3.62 x 10 ⁻²²	cm ³ s ⁻¹	24		
C ₂ H ₅	+	C ₃ H ₇	→	C ₃ H ₈	+	C ₂ H ₄	1.91 x 10 ⁻¹²	cm ³ s ⁻¹	24		
C ₂ H ₅	+	C ₃ H ₇	→	C ₃ H ₆	+	C ₂ H ₆	2.41 x 10 ⁻¹²	cm ³ s ⁻¹	24		
C ₂ H ₅	+	H ₂	→	C ₂ H ₆	+	H	2.97 x 10 ⁻²¹	cm ³ s ⁻¹	22		
C ₂ H ₅	+	H	→	CH ₃	+	CH ₃	5.99 x 10 ⁻¹¹	cm ³ s ⁻¹	23		
C ₂ H ₅	+	H	→	C ₂ H ₄	+	H ₂	3.01 x 10 ⁻¹²	cm ³ s ⁻¹	22		
C ₂ H ₅	+	H	+	M	→	C ₂ H ₆	+	M	2.25 x 10 ⁻¹⁰	cm ³ s ⁻¹	29
C ₂ H ₅	+	H	+	M	→	C ₂ H ₆	+	M	9.20 x 10 ⁻³⁰	cm ⁶ s ⁻¹	^b
C ₂ H ₄	+	C ₂ H	→	C ₂ H ₂	+	C ₂ H ₃	1.40 x 10 ⁻¹⁰	cm ³ s ⁻¹	26		
C ₂ H ₄	+	H	→	C ₂ H ₃	+	H ₂	4.92 x 10 ⁻²¹	cm ³ s ⁻¹	22		
C ₂ H ₄	+	H	+	M	→	C ₂ H ₅	+	M	3.66 x 10 ⁻³⁰	cm ⁶ s ⁻¹	23

C_2H_3	+	C_2H_3		\rightarrow	C_2H_4	+	C_2H_2		1.9×10^{-12}	$\text{cm}^3 \text{s}^{-1}$	22	
C_2H_3	+	C_2H		\rightarrow	C_2H_2	+	C_2H_2		1.9×10^{-12}	$\text{cm}^3 \text{s}^{-1}$	22	
C_2H_3	+	C_3H_8		\rightarrow	C_2H_4	+	C_3H_7		3.40×10^{-21}	$\text{cm}^3 \text{s}^{-1}$	24	
C_2H_3	+	C_3H_7		\rightarrow	C_3H_8	+	C_2H_2		2.01×10^{-12}	$\text{cm}^3 \text{s}^{-1}$	24	
C_2H_3	+	C_3H_7		\rightarrow	C_3H_6	+	C_2H_4		2.01×10^{-12}	$\text{cm}^3 \text{s}^{-1}$	24	
C_2H_3	+	H_2		\rightarrow	C_2H_4	+	H		9.78×10^{-20}	$\text{cm}^3 \text{s}^{-1}$	22	
C_2H_3	+	H		\rightarrow	C_2H_2	+	H_2		2.01×10^{-11}	$\text{cm}^3 \text{s}^{-1}$	23	
C_2H_3	+	H	+	M	\rightarrow	C_2H_4	+	M	2.02×10^{-10}	$\text{cm}^3 \text{s}^{-1}$	29	
									8.26×10^{-30}	$\text{cm}^6 \text{s}^{-1}$	b	
C_2H_2	+	C_2H		\rightarrow	C_4H_2	+	H		1.50×10^{-10}	$\text{cm}^3 \text{s}^{-1}$	30	
C_2H_2	+	H		\rightarrow	C_2H	+	H_2		6.12×10^{-27}	$\text{cm}^3 \text{s}^{-1}$	22	
C_2H_2	+	H	+	M	\rightarrow	C_2H_3	+	M	2.81×10^{-31}	$\text{cm}^6 \text{s}^{-1}$	23	
C_2H	+	C_3H_8		\rightarrow	C_2H_2	+	C_3H_7		5.99×10^{-12}	$\text{cm}^3 \text{s}^{-1}$	24	
C_2H	+	C_3H_7		\rightarrow	C_3H_6	+	C_2H_2		1.00×10^{-11}	$\text{cm}^3 \text{s}^{-1}$	24	
C_2H	+	H_2		\rightarrow	C_2H_2	+	H		1.52×10^{-13}	$\text{cm}^3 \text{s}^{-1}$	22	
C_2H	+	H	+	M	\rightarrow	C_2H_2	+	M	2.31×10^{-10}	$\text{cm}^3 \text{s}^{-1}$	29	
									9.44×10^{-30}	$\text{cm}^6 \text{s}^{-1}$	b	
C_3H_8	+	H		\rightarrow	C_3H_7	+	H_2		5.15×10^{-17}	$\text{cm}^3 \text{s}^{-1}$	24	
C_3H_7	+	C_3H_7		\rightarrow	C_3H_6	+	C_3H_8		2.81×10^{-12}	$\text{cm}^3 \text{s}^{-1}$	24	
C_3H_7	+	H_2		\rightarrow	C_3H_8	+	H		7.12×10^{-21}	$\text{cm}^3 \text{s}^{-1}$	24	
C_3H_7	+	H		\rightarrow	C_3H_6	+	H_2		3.01×10^{-12}	$\text{cm}^3 \text{s}^{-1}$	24	
C_3H_7	+	H	+	M	\rightarrow	C_3H_8	+	M	9.68×10^{-11}	$\text{cm}^3 \text{s}^{-1}$	29	
									3.96×10^{-30}	$\text{cm}^6 \text{s}^{-1}$	b	
C_3H_6	+	H	+	M	\rightarrow	C_3H_7	+	M	9.26×10^{-14}	$\text{cm}^3 \text{s}^{-1}$	31	
									3.79×10^{-33}	$\text{cm}^6 \text{s}^{-1}$	b	
H	+	H	+	M	\rightarrow	H_2	+	M	6.00×10^{-33}	$\text{cm}^6 \text{s}^{-1}$	23	
O	+	O	+	O	\rightarrow	O_2	+	O	5.09×10^{-33}	$\text{cm}^6 \text{s}^{-1}$	32	
O	+	O	+	M	\rightarrow	O_2	+	M	7.19×10^{-33}	$\text{cm}^6 \text{s}^{-1}$	32	
CH_4	+	O		\rightarrow	CH_3	+	OH		5.54×10^{-18}	$\text{cm}^3 \text{s}^{-1}$	23	
CH_3	+	O		\rightarrow	CH_2O	+	H		1.12×10^{-10}	$\text{cm}^3 \text{s}^{-1}$	32	
CH_3	+	O		\rightarrow	CO	+	H_2	+	H	2.80×10^{-11}	$\text{cm}^3 \text{s}^{-1}$	33

CH ₂	+	O	→	CO	+	H ₂	5.53 x 10 ⁻¹¹	cm ³ s ⁻¹	33
CH ₂	+	O	→	CO	+	2H	8.29 x 10 ⁻¹¹	cm ³ s ⁻¹	33
CH ₂	+	O ₂	→	CO ₂	+	H ₂	1.42 x 10 ⁻¹²	cm ³ s ⁻¹	23, 34
CH ₂	+	O ₂	→	CO	+	H ₂ O	1.42 x 10 ⁻¹²	cm ³ s ⁻¹	23, 34
CH ₂	+	O ₂	→	CH ₂ O	+	O	5.39 x 10 ⁻¹³	cm ³ s ⁻¹	23, 34
CH	+	O	→	CO	+	H	6.9 x 10 ⁻¹¹	cm ³ s ⁻¹	23
CH	+	O ₂	→	CO ₂	+	H	1.20 x 10 ⁻¹¹	cm ³ s ⁻¹	33
CH	+	O ₂	→	CO	+	OH	8.00 x 10 ⁻¹²	cm ³ s ⁻¹	33
CH	+	O ₂	→	CHO	+	O	8.00 x 10 ⁻¹²	cm ³ s ⁻¹	33
CH	+	O ₂	→	CO	+	H + O	1.20 x 10 ⁻¹¹	cm ³ s ⁻¹	33
C	+	O ₂	→	CO	+	O	2.45 x 10 ⁻¹³	cm ³ s ⁻¹	35
C ₂ H ₆	+	O	→	C ₂ H ₅	+	OH	5.11 x 10 ⁻¹⁶	cm ³ s ⁻¹	23
C ₂ H ₅	+	O	→	CH ₃ CHO	+	H	8.80 x 10 ⁻¹¹	cm ³ s ⁻¹	33
C ₂ H ₅	+	O	→	CH ₂ O	+	CH ₃	6.9 x 10 ⁻¹¹	cm ³ s ⁻¹	33
C ₂ H ₅	+	O	→	C ₂ H ₄	+	OH	4.40 x 10 ⁻¹¹	cm ³ s ⁻¹	33
C ₂ H ₅	+	O ₂	→	C ₂ H ₄	+	HO ₂	3.80 x 10 ⁻¹⁵	cm ³ s ⁻¹	36
C ₂ H ₅	+	O ₂ + CH ₄	→	C ₂ H ₅ O ₂	+	CH ₄	5.75 x 10 ⁻²⁹	cm ⁶ s ⁻¹	36
C ₂ H ₄	+	O	→	CH ₂ CHO	+	H	2.63 x 10 ⁻¹³	cm ³ s ⁻¹	33
C ₂ H ₄	+	O	→	CHO	+	CH ₃	4.51 x 10 ⁻¹³	cm ³ s ⁻¹	33
C ₂ H ₃	+	O	→	C ₂ H ₂	+	OH	1.25 x 10 ⁻¹¹	cm ³ s ⁻¹	33
C ₂ H ₃	+	O	→	CO	+	CH ₃	1.25 x 10 ⁻¹¹	cm ³ s ⁻¹	33
C ₂ H ₃	+	O	→	CHO	+	CH ₂	1.25 x 10 ⁻¹¹	cm ³ s ⁻¹	33
C ₂ H ₃	+	O	→	CH ₂ CO	+	H	1.25 x 10 ⁻¹¹	cm ³ s ⁻¹	33
C ₂ H ₃	+	O ₂	→	CH ₂ O	+	CHO	9.00 x 10 ⁻¹²	cm ³ s ⁻¹	23
C ₂ H ₂	+	O	→	CH ₂	+	CO	6.75 x 10 ⁻¹⁴	cm ³ s ⁻¹	23
C ₂ H ₂	+	O	→	C ₂ HO	+	H	6.75 x 10 ⁻¹⁴	cm ³ s ⁻¹	23
C ₂ H	+	O	→	CH	+	CO	1.70 x 10 ⁻¹¹	cm ³ s ⁻¹	23
C ₂ H	+	O ₂	→	CHO	+	CO	3.00 x 10 ⁻¹¹	cm ³ s ⁻¹	23
C ₂ H	+	O ₂	→	C ₂ HO	+	O	1.00 x 10 ⁻¹²	cm ³ s ⁻¹	22
C ₃ H ₈	+	O	→	C ₃ H ₇	+	OH	2.73 x 10 ⁻¹⁵	cm ³ s ⁻¹	24
H ₂	+	O	→	OH	+	H	9.32 x 10 ⁻¹⁸	cm ³ s ⁻¹	23

H	+	O	+	CH ₄	→	OH	+	CH ₄	4.33 x 10 ⁻³²	cm ⁶ s ⁻¹	22
H	+	O ₂			→	OH	+	O	1.87 x 10 ⁻²²	cm ³ s ⁻¹	23
H	+	O ₂	+	CH ₄	→	HO ₂	+	CH ₄	5.40 x 10 ⁻³²	cm ⁶ s ⁻¹	37
CH ₄	+	OH			→	CH ₃	+	H ₂ O	6.62 x 10 ⁻¹⁵	cm ³ s ⁻¹	36
CH ₄	+	HO ₂			→	CH ₃	+	H ₂ O ₂	8.76 x 10 ⁻²⁷	cm ³ s ⁻¹	22
CH ₄	+	CHO			→	CH ₃	+	CH ₂ O	6.07 x 10 ⁻³⁰	cm ³ s ⁻¹	22
CH ₄	+	CH ₃ O			→	CH ₃ OH	+	CH ₃	9.42 x 10 ⁻²⁰	cm ³ s ⁻¹	22
CH ₃	+	CO	+	CH ₄	→	CH ₃ CO	+	CH ₄	4.19 x 10 ⁻³⁶	cm ⁶ s ⁻¹	30
CH ₃	+	H ₂ O			→	CH ₄	+	OH	1.82 x 10 ⁻²⁵	cm ³ s ⁻¹	22
CH ₃	+	OH			→	CH ₂	+	H ₂ O	1.13 x 10 ⁻¹²	cm ³ s ⁻¹	30
CH ₃	+	OH			→	CH ₂ OH	+	H	1.31 x 10 ⁻¹¹	cm ³ s ⁻¹	38
CH ₃	+	OH			→	CH ₃ O	+	H	1.9 x 10 ⁻¹⁰	cm ³ s ⁻¹	38
CH ₃	+	OH	+	M	→	CH ₃ OH	+	M	2.30 x 10 ⁻²⁷	cm ⁶ s ⁻¹	30
CH ₃	+	HO ₂			→	CH ₃ O	+	OH	3.00 x 10 ⁻¹¹	cm ³ s ⁻¹	23
CH ₃	+	HO ₂			→	CH ₄	+	O ₂	5.99 x 10 ⁻¹²	cm ³ s ⁻¹	22
CH ₃	+	CH ₂ O			→	CH ₄	+	CHO	6.14 x 10 ⁻¹⁸	cm ³ s ⁻¹	30
CH ₃	+	CHO			→	CH ₄	+	CO	2.00 x 10 ⁻¹⁰	cm ³ s ⁻¹	22
CH ₃	+	CH ₃ O			→	CH ₄	+	CH ₂ O	4.00 x 10 ⁻¹¹	cm ³ s ⁻¹	22
CH ₃	+	CH ₃ CHO			→	CH ₄	+	CH ₃ CO	4.95 x 10 ⁻¹⁸	cm ³ s ⁻¹	23
CH ₂	+	CO ₂			→	CH ₂ O	+	CO	3.90 x 10 ⁻¹⁴	cm ³ s ⁻¹	22
CH ₂	+	H ₂ O			→	CH ₃	+	OH	1.9 x 10 ⁻¹⁶	cm ³ s ⁻¹	22
CH ₂	+	OH			→	CH ₂ O	+	H	3.00 x 10 ⁻¹¹	cm ³ s ⁻¹	22
CH ₂	+	HO ₂			→	CH ₂ O	+	OH	3.00 x 10 ⁻¹¹	cm ³ s ⁻¹	22
CH ₂	+	CH ₂ O			→	CH ₃	+	CHO	1.00 x 10 ⁻¹⁴	cm ³ s ⁻¹	22
CH ₂	+	CHO			→	CH ₃	+	CO	3.00 x 10 ⁻¹¹	cm ³ s ⁻¹	22
CH ₂	+	CH ₃ O			→	CH ₃	+	CH ₂ O	3.00 x 10 ⁻¹¹	cm ³ s ⁻¹	22
CH	+	CO ₂			→	CHO	+	CO	9.68 x 10 ⁻¹³	cm ³ s ⁻¹	33
CH	+	CO ₂			→	2CO	+	H	9.68 x 10 ⁻¹³	cm ³ s ⁻¹	33
CH	+	CO	+	M	→	C ₂ HO	+	M	4.04 x 10 ⁻³⁰	cm ⁶ s ⁻¹	33
C ₂ H ₆	+	OH			→	C ₂ H ₅	+	H ₂ O	2.46 x 10 ⁻¹³	cm ³ s ⁻¹	36
C ₂ H ₆	+	HO ₂			→	C ₂ H ₅	+	H ₂ O ₂	6.36 x 10 ⁻²⁴	cm ³ s ⁻¹	22

C_2H_6	+	CHO	\rightarrow	C_2H_5	+	CH_2O	2.19×10^{-26}	$\text{cm}^3 \text{s}^{-1}$	22
C_2H_6	+	CH_3O	\rightarrow	C_2H_5	+	CH_3OH	2.72×10^{-18}	$\text{cm}^3 \text{s}^{-1}$	22
C_2H_5	+	OH	\rightarrow	C_2H_4	+	H_2O	4.00×10^{-11}	$\text{cm}^3 \text{s}^{-1}$	22
C_2H_5	+	HO_2	\rightarrow	C_2H_6	+	O_2	5.00×10^{-13}	$\text{cm}^3 \text{s}^{-1}$	22
C_2H_5	+	HO_2	\rightarrow	C_2H_4	+	H_2O_2	5.00×10^{-13}	$\text{cm}^3 \text{s}^{-1}$	22
C_2H_5	+	CH_2O	\rightarrow	C_2H_6	+	CHO	4.47×10^{-18}	$\text{cm}^3 \text{s}^{-1}$	22
C_2H_5	+	CHO	\rightarrow	C_2H_6	+	CO	2.00×10^{-10}	$\text{cm}^3 \text{s}^{-1}$	22
C_2H_5	+	CH_3O	\rightarrow	C_2H_6	+	CH_2O	4.00×10^{-11}	$\text{cm}^3 \text{s}^{-1}$	22
C_2H_4	+	OH	\rightarrow	C_2H_3	+	H_2O	1.54×10^{-16}	$\text{cm}^3 \text{s}^{-1}$	22
C_2H_4	+	HO_2	\rightarrow	CH_3CHO	+	OH	1.62×10^{-20}	$\text{cm}^3 \text{s}^{-1}$	22
C_2H_3	+	H_2O	\rightarrow	C_2H_4	+	OH	1.82×10^{-25}	$\text{cm}^3 \text{s}^{-1}$	22
C_2H_3	+	OH	\rightarrow	C_2H_2	+	H_2O	5.00×10^{-11}	$\text{cm}^3 \text{s}^{-1}$	22
C_2H_3	+	CH_2O	\rightarrow	C_2H_4	+	CHO	4.41×10^{-18}	$\text{cm}^3 \text{s}^{-1}$	22
C_2H_3	+	CHO	\rightarrow	C_2H_4	+	CO	1.50×10^{-10}	$\text{cm}^3 \text{s}^{-1}$	22
C_2H_3	+	CH_3O	\rightarrow	C_2H_4	+	CH_2O	4.00×10^{-11}	$\text{cm}^3 \text{s}^{-1}$	22
C_2H_2	+	OH	\rightarrow	C_2H	+	H_2O	1.77×10^{-22}	$\text{cm}^3 \text{s}^{-1}$	22
C_2H_2	+	HO_2	\rightarrow	CH_2CO	+	OH	1.62×10^{-20}	$\text{cm}^3 \text{s}^{-1}$	22
C_2H	+	OH	\rightarrow	CH_2	+	CO	3.00×10^{-11}	$\text{cm}^3 \text{s}^{-1}$	22
C_2H	+	OH	\rightarrow	C_2H_2	+	O	3.00×10^{-11}	$\text{cm}^3 \text{s}^{-1}$	22
C_2H	+	HO_2	\rightarrow	C_2H_2	+	O_2	3.00×10^{-11}	$\text{cm}^3 \text{s}^{-1}$	22
C_2H	+	HO_2	\rightarrow	C_2HO	+	OH	3.00×10^{-11}	$\text{cm}^3 \text{s}^{-1}$	22
C_2H	+	CHO	\rightarrow	C_2H_2	+	CO	1.00×10^{-10}	$\text{cm}^3 \text{s}^{-1}$	22
C_2H	+	CH_3O	\rightarrow	C_2H_2	+	CH_2O	4.00×10^{-11}	$\text{cm}^3 \text{s}^{-1}$	22
C_3H_8	+	OH	\rightarrow	C_3H_7	+	H_2O	3.76×10^{-15}	$\text{cm}^3 \text{s}^{-1}$	24
C_3H_8	+	CH_3O	\rightarrow	C_3H_7	+	CH_3OH	1.42×10^{-17}	$\text{cm}^3 \text{s}^{-1}$	24
C_3H_7	+	CH_2O	\rightarrow	C_3H_8	+	CHO	4.10×10^{-18}	$\text{cm}^3 \text{s}^{-1}$	24
C_3H_7	+	CHO	\rightarrow	C_3H_8	+	CO	1.00×10^{-10}	$\text{cm}^3 \text{s}^{-1}$	24
C_3H_7	+	CH_3O	\rightarrow	C_3H_8	+	CH_2O	4.00×10^{-11}	$\text{cm}^3 \text{s}^{-1}$	24
H_2	+	OH	\rightarrow	H	+	H_2O	7.02×10^{-15}	$\text{cm}^3 \text{s}^{-1}$	37
H_2	+	CHO	\rightarrow	H	+	CH_2O	2.78×10^{-26}	$\text{cm}^3 \text{s}^{-1}$	22
H	+	CO_2	\rightarrow	CO	+	OH	1.40×10^{-29}	$\text{cm}^3 \text{s}^{-1}$	22

H	+	CO	+	M	→	CHO	+	M	1.54×10^{-34}	$\text{cm}^6 \text{s}^{-1}$	30
H	+	H ₂ O			→	H ₂	+	OH	5.86×10^{-26}	$\text{cm}^3 \text{s}^{-1}$	23
H	+	OH			→	H ₂	+	O	1.05×10^{-16}	$\text{cm}^3 \text{s}^{-1}$	22
H	+	OH	+	M	→	H ₂ O	+	M	4.33×10^{-30}	$\text{cm}^6 \text{s}^{-1}$	23
H	+	HO ₂			→	H ₂	+	O ₂	5.9×10^{-12}	$\text{cm}^3 \text{s}^{-1}$	37
H	+	HO ₂			→	H ₂ O	+	O	2.40×10^{-12}	$\text{cm}^3 \text{s}^{-1}$	37
H	+	HO ₂			→	OH	+	OH	7.20×10^{-11}	$\text{cm}^3 \text{s}^{-1}$	37
H	+	CH ₂ O			→	H ₂	+	CHO	5.72×10^{-14}	$\text{cm}^3 \text{s}^{-1}$	30
H	+	CHO			→	H ₂	+	CO	1.50×10^{-10}	$\text{cm}^3 \text{s}^{-1}$	23
H	+	CH ₃ O			→	H ₂	+	CH ₂ O	2.32×10^{-11}	$\text{cm}^3 \text{s}^{-1}$	33
H	+	CH ₃ O			→	CH ₃	+	OH	9.93×10^{-12}	$\text{cm}^3 \text{s}^{-1}$	33
H	+	CH ₃ CHO			→	H ₂	+	CH ₃ CO	8.98×10^{-14}	$\text{cm}^3 \text{s}^{-1}$	23
H	+	CH ₂ CO			→	CH ₃	+	CO	1.04×10^{-13}	$\text{cm}^3 \text{s}^{-1}$	23
H	+	C ₂ HO			→	CH ₂	+	CO	2.50×10^{-10}	$\text{cm}^3 \text{s}^{-1}$	23
O	+	CO	+	M	→	CO ₂	+	M	1.11×10^{-35}	$\text{cm}^6 \text{s}^{-1}$	22
O	+	H ₂ O			→	OH	+	OH	4.48×10^{-24}	$\text{cm}^3 \text{s}^{-1}$	22
O	+	OH			→	H	+	O ₂	3.46×10^{-11}	$\text{cm}^3 \text{s}^{-1}$	37
O	+	HO ₂			→	O ₂	+	OH	5.70×10^{-11}	$\text{cm}^3 \text{s}^{-1}$	37
O	+	CH ₂ O			→	OH	+	CHO	1.73×10^{-13}	$\text{cm}^3 \text{s}^{-1}$	23
O	+	CHO			→	CO	+	OH	5.00×10^{-11}	$\text{cm}^3 \text{s}^{-1}$	23
O	+	CHO			→	H	+	CO ₂	5.00×10^{-11}	$\text{cm}^3 \text{s}^{-1}$	23
O	+	CH ₃ O			→	CH ₃	+	O ₂	2.20×10^{-11}	$\text{cm}^3 \text{s}^{-1}$	23
O	+	CH ₃ O			→	OH	+	CH ₂ O	3.00×10^{-12}	$\text{cm}^3 \text{s}^{-1}$	23
O	+	CH ₃ CHO			→	OH	+	CH ₃ CO	4.68×10^{-13}	$\text{cm}^3 \text{s}^{-1}$	23
O	+	CH ₂ CO			→	CH ₂	+	CO ₂	2.29×10^{-13}	$\text{cm}^3 \text{s}^{-1}$	23, 39
O	+	CH ₂ CO			→	CH ₂ O	+	CO	7.88×10^{-14}	$\text{cm}^3 \text{s}^{-1}$	23, 39
O	+	CH ₂ CO			→	CHO	+	CO	4.33×10^{-14}	$\text{cm}^3 \text{s}^{-1}$	23, 39
O	+	CH ₂ CO			→	CHO	+	CHO	4.33×10^{-14}	$\text{cm}^3 \text{s}^{-1}$	23, 39
O	+	C ₂ HO			→	CO	+	CO	1.9×10^{-10}	$\text{cm}^3 \text{s}^{-1}$	23
O ₂	+	CHO			→	CO	+	HO ₂	5.10×10^{-12}	$\text{cm}^3 \text{s}^{-1}$	36
O ₂	+	CH ₃ O			→	CH ₂ O	+	HO ₂	1.97×10^{-15}	$\text{cm}^3 \text{s}^{-1}$	36

O ₂	+	CH ₂ CHO	→	CH ₂ O	+	CO	+	OH	3.00 x 10 ⁻¹⁴	cm ³ s ⁻¹	23,40,41
O ₂	+	C ₂ HO	→	CO	+	CO	+	OH	6.46 x 10 ⁻¹³	cm ³ s ⁻¹	23
CO	+	OH	→	CO ₂	+	H			1.25 x 10 ⁻¹³	cm ³ s ⁻¹	23
CO	+	CH ₃ O	→	CO ₂	+	CH ₃			6.56 x 10 ⁻²⁰	cm ³ s ⁻¹	22
H ₂ O	+	CH ₃ O	→	CH ₃ OH	+	OH			1.67 x 10 ⁻¹⁴	cm ³ s ⁻¹	42
OH	+	OH	→	H ₂ O	+	O			1.47 x 10 ⁻¹²	cm ³ s ⁻¹	37
OH	+	OH	+	M	→	H ₂ O ₂	+	M	6.86 x 10 ⁻³¹	cm ⁶ s ⁻¹	37
OH	+	HO ₂	→	O ₂	+	H ₂ O			1.10 x 10 ⁻¹⁰	cm ³ s ⁻¹	37
OH	+	CH ₂ O	→	H ₂ O	+	CHO			8.47 x 10 ⁻¹²	cm ³ s ⁻¹	36
OH	+	CHO	→	CO	+	H ₂ O			1.70 x 10 ⁻¹⁰	cm ³ s ⁻¹	23
OH	+	CH ₃ O	→	CH ₂ O	+	H ₂ O			3.00 x 10 ⁻¹¹	cm ³ s ⁻¹	22
OH	+	CH ₃ CHO	→	CH ₃ CO	+	H ₂ O			1.49 x 10 ⁻¹¹	cm ³ s ⁻¹	36
OH	+	CH ₂ CO	→	CO	+	CH ₂ OH			1.14 x 10 ⁻¹¹	cm ³ s ⁻¹	23, 43
HO ₂	+	HO ₂	→	H ₂ O ₂	+	O ₂			1.63 x 10 ⁻¹²	cm ³ s ⁻¹	37
HO ₂	+	CH ₂ O	→	CHO	+	H ₂ O ₂			1.05 x 10 ⁻²⁰	cm ³ s ⁻¹	22
HO ₂	+	CHO	→	OH	+	H	+	CO ₂	5.00 x 10 ⁻¹¹	cm ³ s ⁻¹	22
HO ₂	+	CH ₃ O	→	CH ₂ O	+	H ₂ O ₂			5.00 x 10 ⁻¹³	cm ³ s ⁻¹	22
CH ₂ O	+	CH ₃ O	→	CH ₃ OH	+	CHO			1.14 x 10 ⁻¹⁵	cm ³ s ⁻¹	22
CHO	+	CHO	→	CH ₂ O	+	CO			5.00 x 10 ⁻¹¹	cm ³ s ⁻¹	23
CHO	+	CH ₃ O	→	CH ₃ OH	+	CO			1.50 x 10 ⁻¹⁰	cm ³ s ⁻¹	22
CH ₃ O	+	CH ₃ O	→	CH ₂ O	+	CH ₃ OH			1.00 x 10 ⁻¹⁰	cm ³ s ⁻¹	22
CH ₄	+	CH ₃ CO	→	CH ₃ CHO	+	CH ₃			1.14 x 10 ⁻²⁹	cm ³ s ⁻¹	22
CH ₄	+	CH ₂ OH	→	CH ₃ OH	+	CH ₃			2.55 x 10 ⁻²⁷	cm ³ s ⁻¹	44
CH ₃	+	H ₂ O ₂	→	CH ₄	+	HO ₂			5.46 x 10 ⁻¹⁴	cm ³ s ⁻¹	22
CH ₃	+	CH ₃ OH	→	CH ₄	+	CH ₃ O			1.01 x 10 ⁻²⁰	cm ³ s ⁻¹	44
CH ₃	+	CH ₃ OH	→	CH ₄	+	CH ₂ OH			2.66 x 10 ⁻²⁰	cm ³ s ⁻¹	44
CH ₃	+	CH ₂ OH	→	CH ₄	+	CH ₂ O			4.00 x 10 ⁻¹²	cm ³ s ⁻¹	44
CH ₂	+	H ₂ O ₂	→	CH ₃	+	HO ₂			1.00 x 10 ⁻¹⁴	cm ³ s ⁻¹	22
CH ₂	+	CH ₃ CO	→	CH ₂ CO	+	CH ₃			3.00 x 10 ⁻¹¹	cm ³ s ⁻¹	22
CH ₂	+	CH ₃ OH	→	CH ₃ O	+	CH ₃			1.01 x 10 ⁻²⁰	cm ³ s ⁻¹	44
CH ₂	+	CH ₃ OH	→	CH ₂ OH	+	CH ₃			2.66 x 10 ⁻²⁰	cm ³ s ⁻¹	44

CH ₂	+	CH ₂ OH	→	CH ₂ O	+	CH ₃	2.00 x 10 ⁻¹²	cm ³ s ⁻¹	44
CH ₂	+	CH ₂ OH	→	C ₂ H ₄	+	OH	4.00 x 10 ⁻¹¹	cm ³ s ⁻¹	44
C ₂ H ₅	+	H ₂ O ₂	→	C ₂ H ₆	+	HO ₂	2.83 x 10 ⁻¹⁵	cm ³ s ⁻¹	22
C ₂ H ₅	+	CH ₃ OH	→	C ₂ H ₆	+	CH ₃ O	3.50 x 10 ⁻²²	cm ³ s ⁻¹	44
C ₂ H ₅	+	CH ₃ OH	→	C ₂ H ₆	+	CH ₂ OH	9.49 x 10 ⁻²²	cm ³ s ⁻¹	44
C ₂ H ₅	+	CH ₂ OH	→	C ₂ H ₆	+	CH ₂ O	4.00 x 10 ⁻¹²	cm ³ s ⁻¹	44
C ₂ H ₅	+	CH ₂ OH	→	CH ₃ OH	+	C ₂ H ₄	4.00 x 10 ⁻¹²	cm ³ s ⁻¹	44
C ₂ H ₃	+	H ₂ O ₂	→	C ₂ H ₄	+	HO ₂	5.46 x 10 ⁻¹⁴	cm ³ s ⁻¹	22
C ₂ H ₃	+	CH ₃ OH	→	C ₂ H ₄	+	CH ₃ O	1.01 x 10 ⁻²⁰	cm ³ s ⁻¹	44
C ₂ H ₃	+	CH ₃ OH	→	C ₂ H ₄	+	CH ₂ OH	2.66 x 10 ⁻²⁰	cm ³ s ⁻¹	44
C ₂ H ₃	+	CH ₂ OH	→	C ₂ H ₄	+	CH ₂ O	5.00 x 10 ⁻¹¹	cm ³ s ⁻¹	44
C ₂ H ₂	+	CH ₂ OH	→	C ₂ H ₃	+	CH ₂ O	3.32 x 10 ⁻¹⁹	cm ³ s ⁻¹	44
C ₂ H	+	CH ₃ OH	→	C ₂ H ₂	+	CH ₃ O	2.00 x 10 ⁻¹²	cm ³ s ⁻¹	44
C ₂ H	+	CH ₃ OH	→	C ₂ H ₂	+	CH ₂ OH	1.00 x 10 ⁻¹¹	cm ³ s ⁻¹	44
C ₂ H	+	CH ₂ OH	→	C ₂ H ₂	+	CH ₂ O	5.99 x 10 ⁻¹¹	cm ³ s ⁻¹	44
C ₃ H ₇	+	OH	→	C ₃ H ₆	+	H ₂ O	4.00 x 10 ⁻¹¹	cm ³ s ⁻¹	24
C ₃ H ₇	+	H ₂ O ₂	→	C ₃ H ₈	+	HO ₂	7.08 x 10 ⁻¹⁷	cm ³ s ⁻¹	24
C ₃ H ₇	+	CH ₃ OH	→	C ₃ H ₈	+	CH ₃ O	3.51 x 10 ⁻²²	cm ³ s ⁻¹	24
C ₃ H ₇	+	CH ₃ OH	→	C ₃ H ₈	+	CH ₂ OH	8.45 x 10 ⁻²²	cm ³ s ⁻¹	24
C ₃ H ₇	+	CH ₂ OH	→	C ₃ H ₈	+	CH ₂ O	1.9 x 10 ⁻¹²	cm ³ s ⁻¹	24
C ₃ H ₇	+	CH ₂ OH	→	C ₃ H ₆	+	CH ₃ OH	8.00 x 10 ⁻¹³	cm ³ s ⁻¹	24
H	+	H ₂ O ₂	→	H ₂ O	+	OH	4.20 x 10 ⁻¹⁴	cm ³ s ⁻¹	23
H	+	H ₂ O ₂	→	H ₂	+	HO ₂	5.15 x 10 ⁻¹⁵	cm ³ s ⁻¹	23
H	+	CH ₃ OH	→	CH ₂ OH	+	H ₂	1.27 x 10 ⁻¹⁵	cm ³ s ⁻¹	44
H	+	CH ₃ OH	→	CH ₃ O	+	H ₂	3.18 x 10 ⁻¹⁶	cm ³ s ⁻¹	44
H	+	CH ₂ OH	→	CH ₂ O	+	H ₂	1.00 x 10 ⁻¹¹	cm ³ s ⁻¹	44
H	+	CH ₂ OH	→	CH ₃	+	OH	1.9 x 10 ⁻¹⁰	cm ³ s ⁻¹	44
H	+	CH ₂ OH	+	M	→	CH ₃ OH	+	M	2.89 x 10 ⁻¹⁰ cm ³ s ⁻¹
									1.18 x 10 ⁻²⁹ cm ⁶ s ⁻¹
O	+	H ₂ O ₂	→	HO ₂	+	OH	8.91 x 10 ⁻¹⁶	cm ³ s ⁻¹	33
O	+	H ₂ O ₂	→	O ₂	+	H ₂ O	8.91 x 10 ⁻¹⁶	cm ³ s ⁻¹	33

O	+	CH ₃ CO	→	OH	+	CH ₂ CO	8.75 x 10 ⁻¹¹	cm ³ s ⁻¹	33	
O	+	CH ₃ CO	→	CO ₂	+	CH ₃	2.63 x 10 ⁻¹⁰	cm ³ s ⁻¹	33	
O	+	CH ₃ OH	→	OH	+	CH ₂ OH	1.12 x 10 ⁻¹⁴	cm ³ s ⁻¹	46	
O	+	CH ₃ OH	→	OH	+	CH ₃ O	1.68 x 10 ⁻¹⁵	cm ³ s ⁻¹	46	
O	+	CH ₂ OH	→	CH ₂ O	+	OH	7.00 x 10 ⁻¹¹	cm ³ s ⁻¹	44	
O ₂	+	CH ₂ OH	→	CH ₂ O	+	HO ₂	9.70 x 10 ⁻¹²	cm ³ s ⁻¹	36	
OH	+	H ₂ O ₂	→	HO ₂	+	H ₂ O	1.70 x 10 ⁻¹²	cm ³ s ⁻¹	37	
OH	+	CH ₃ CO	→	CH ₂ CO	+	H ₂ O	2.00 x 10 ⁻¹¹	cm ³ s ⁻¹	22	
OH	+	CH ₃ CO	→	CH ₃	+	CO	+ OH	5.00 x 10 ⁻¹¹	cm ³ s ⁻¹	22
OH	+	CH ₃ OH	→	H ₂ O	+	CH ₂ OH	7.67 x 10 ⁻¹³	cm ³ s ⁻¹	36	
OH	+	CH ₃ OH	→	H ₂ O	+	CH ₃ O	1.35 x 10 ⁻¹³	cm ³ s ⁻¹	36	
OH	+	CH ₂ OH	→	CH ₂ O	+	H ₂ O	4.00 x 10 ⁻¹¹	cm ³ s ⁻¹	44	
HO ₂	+	CH ₃ CO	→	CH ₃	+	CO ₂	+ OH	5.00 x 10 ⁻¹¹	cm ³ s ⁻¹	22
HO ₂	+	CH ₃ OH	→	CH ₂ OH	+	H ₂ O ₂	1.10 x 10 ⁻²²	cm ³ s ⁻¹	44	
HO ₂	+	CH ₂ OH	→	CH ₂ O	+	H ₂ O ₂	2.00 x 10 ⁻¹¹	cm ³ s ⁻¹	44	
CH ₂ O	+	CH ₃ CO	→	CH ₃ CHO	+	CHO	1.17 x 10 ⁻²²	cm ³ s ⁻¹	22	
CH ₂ O	+	CH ₂ OH	→	CH ₃ OH	+	CHO	4.22 x 10 ⁻¹⁸	cm ³ s ⁻¹	44	
CHO	+	H ₂ O ₂	→	CH ₂ O	+	HO ₂	1.50 x 10 ⁻¹⁸	cm ³ s ⁻¹	22	
CHO	+	CH ₃ CO	→	CH ₃ CHO	+	CO	1.50 x 10 ⁻¹¹	cm ³ s ⁻¹	22	
CHO	+	CH ₃ OH	→	CH ₂ O	+	CH ₂ OH	6.85 x 10 ⁻²³	cm ³ s ⁻¹	44	
CHO	+	CH ₂ OH	→	CH ₂ O	+	CH ₂ O	3.00 x 10 ⁻¹⁰	cm ³ s ⁻¹	44	
CHO	+	CH ₂ OH	→	CH ₃ OH	+	CO	2.00 x 10 ⁻¹⁰	cm ³ s ⁻¹	44	
CH ₃ O	+	CH ₃ CO	→	CH ₃ OH	+	CH ₂ CO	1.00 x 10 ⁻¹¹	cm ³ s ⁻¹	22	
CH ₃ O	+	CH ₃ OH	→	CH ₃ OH	+	CH ₂ OH	5.38 x 10 ⁻¹⁶	cm ³ s ⁻¹	44	
CH ₃ O	+	CH ₂ OH	→	CH ₂ O	+	CH ₃ OH	4.00 x 10 ⁻¹¹	cm ³ s ⁻¹	44	
H ₂ O ₂	+	CH ₃ CO	→	CH ₃ CHO	+	HO ₂	3.05 x 10 ⁻¹⁹	cm ³ s ⁻¹	22	
H ₂ O ₂	+	CH ₂ OH	→	CH ₃ OH	+	HO ₂	6.56 x 10 ⁻¹⁷	cm ³ s ⁻¹	44	
CH ₃ CO	+	CH ₃ OH	→	CH ₃ CHO	+	CH ₂ OH	2.22 x 10 ⁻²²	cm ³ s ⁻¹	44	
CH ₂ OH	+	CH ₂ OH	→	CH ₂ O	+	CH ₃ OH	8.00 x 10 ⁻¹²	cm ³ s ⁻¹	44	

Table 4: Ion-neutral and ion-ion reactions included in the model, as well as the corresponding rate coefficients and the references where these data were adopted from.

CH_5^+	+	CH_2	\rightarrow	CH_3^+	+	CH_4	$9.9 \times 10^{-10} \text{ cm}^3 \text{ s}^{-1}$	47
CH_5^+	+	CH	\rightarrow	CH_2^+	+	CH_4	$6.90 \times 10^{-10} \text{ cm}^3 \text{ s}^{-1}$	47
CH_5^+	+	C	\rightarrow	CH^+	+	CH_4	$1.20 \times 10^{-09} \text{ cm}^3 \text{ s}^{-1}$	47
CH_5^+	+	C_2H_6	\rightarrow	C_2H_5^+	+	$\text{H}_2 + \text{CH}_4$	$2.25 \times 10^{-10} \text{ cm}^3 \text{ s}^{-1}$	48
CH_5^+	+	C_2H_4	\rightarrow	C_2H_5^+	+	CH_4	$1.50 \times 10^{-09} \text{ cm}^3 \text{ s}^{-1}$	47
CH_5^+	+	C_2H_2	\rightarrow	C_2H_3^+	+	CH_4	$1.9 \times 10^{-09} \text{ cm}^3 \text{ s}^{-1}$	47
CH_5^+	+	C_2H	\rightarrow	C_2H_2^+	+	CH_4	$9.00 \times 10^{-10} \text{ cm}^3 \text{ s}^{-1}$	47
CH_5^+	+	H	\rightarrow	CH_4^+	+	H_2	$1.50 \times 10^{-10} \text{ cm}^3 \text{ s}^{-1}$	47
CH_5^+	+	O	\rightarrow	H_3O^+	+	CH_2	$2.20 \times 10^{-10} \text{ cm}^3 \text{ s}^{-1}$	47
CH_5^+	+	H_2O	\rightarrow	H_3O^+	+	CH_4	$3.70 \times 10^{-09} \text{ cm}^3 \text{ s}^{-1}$	47
CH_4^+	+	CH_4	\rightarrow	CH_5^+	+	CH_3	$1.50 \times 10^{-09} \text{ cm}^3 \text{ s}^{-1}$	47
CH_4^+	+	C_2H_6	\rightarrow	C_2H_4^+	+	$\text{CH}_4 + \text{H}_2$	$1.91 \times 10^{-09} \text{ cm}^3 \text{ s}^{-1}$	48
CH_4^+	+	C_2H_4	\rightarrow	C_2H_5^+	+	CH_3	$4.23 \times 10^{-10} \text{ cm}^3 \text{ s}^{-1}$	47
CH_4^+	+	C_2H_4	\rightarrow	C_2H_4^+	+	CH_4	$1.38 \times 10^{-09} \text{ cm}^3 \text{ s}^{-1}$	47
CH_4^+	+	C_2H_2	\rightarrow	C_2H_3^+	+	CH_3	$1.23 \times 10^{-09} \text{ cm}^3 \text{ s}^{-1}$	47
CH_4^+	+	C_2H_2	\rightarrow	C_2H_2^+	+	CH_4	$1.13 \times 10^{-09} \text{ cm}^3 \text{ s}^{-1}$	47
CH_4^+	+	H_2	\rightarrow	CH_5^+	+	H	$3.30 \times 10^{-11} \text{ cm}^3 \text{ s}^{-1}$	47
CH_4^+	+	H	\rightarrow	CH_3^+	+	H_2	$1.00 \times 10^{-11} \text{ cm}^3 \text{ s}^{-1}$	47
CH_4^+	+	O	\rightarrow	CH_3^+	+	OH	$1.00 \times 10^{-09} \text{ cm}^3 \text{ s}^{-1}$	47
CH_4^+	+	O_2	\rightarrow	O_2^+	+	CH_4	$3.90 \times 10^{-10} \text{ cm}^3 \text{ s}^{-1}$	47
CH_4^+	+	H_2O	\rightarrow	H_3O^+	+	CH_3	$2.9 \times 10^{-09} \text{ cm}^3 \text{ s}^{-1}$	47
CH_3^+	+	CH_4	\rightarrow	CH_4^+	+	CH_3	$1.36 \times 10^{-10} \text{ cm}^3 \text{ s}^{-1}$	49
CH_3^+	+	CH_4	\rightarrow	C_2H_5^+	+	H_2	$1.20 \times 10^{-09} \text{ cm}^3 \text{ s}^{-1}$	47
CH_3^+	+	CH_2	\rightarrow	C_2H_3^+	+	H_2	$9.90 \times 10^{-10} \text{ cm}^3 \text{ s}^{-1}$	47
CH_3^+	+	CH	\rightarrow	C_2H_2^+	+	H_2	$7.10 \times 10^{-10} \text{ cm}^3 \text{ s}^{-1}$	47
CH_3^+	+	C_2H_6	\rightarrow	C_2H_5^+	+	CH_4	$1.48 \times 10^{-09} \text{ cm}^3 \text{ s}^{-1}$	47

CH_3^+	+	C_2H_4	\rightarrow	C_2H_3^+	+	CH_4	3.50×10^{-10}	$\text{cm}^3 \text{s}^{-1}$	47
CH_3^+	+	C_2H_3	\rightarrow	C_2H_3^+	+	CH_3	3.00×10^{-10}	$\text{cm}^3 \text{s}^{-1}$	47
CH_2^+	+	CH_4	\rightarrow	CH_3^+	+	CH_3	1.38×10^{-10}	$\text{cm}^3 \text{s}^{-1}$	50
CH_2^+	+	CH_4	\rightarrow	C_2H_5^+	+	H	3.9×10^{-10}	$\text{cm}^3 \text{s}^{-1}$	47
CH_2^+	+	CH_4	\rightarrow	C_2H_4^+	+	H_2	8.40×10^{-10}	$\text{cm}^3 \text{s}^{-1}$	47
CH_2^+	+	CH_4	\rightarrow	C_2H_3^+	+	$\text{H}_2 + \text{H}$	2.31×10^{-10}	$\text{cm}^3 \text{s}^{-1}$	50
CH_2^+	+	CH_4	\rightarrow	C_2H_2^+	+	2H_2	3.97×10^{-10}	$\text{cm}^3 \text{s}^{-1}$	50
CH_2^+	+	H_2	\rightarrow	CH_3^+	+	H	1.9×10^{-09}	$\text{cm}^3 \text{s}^{-1}$	47
CH^+	+	CH_4	\rightarrow	C_2H_4^+	+	H	6.50×10^{-11}	$\text{cm}^3 \text{s}^{-1}$	47
CH^+	+	CH_4	\rightarrow	C_2H_3^+	+	H_2	1.09×10^{-09}	$\text{cm}^3 \text{s}^{-1}$	47
CH^+	+	CH_4	\rightarrow	C_2H_2^+	+	$\text{H}_2 + \text{H}$	1.43×10^{-10}	$\text{cm}^3 \text{s}^{-1}$	47
CH^+	+	H_2	\rightarrow	CH_2^+	+	H	1.20×10^{-09}	$\text{cm}^3 \text{s}^{-1}$	47
CH^+	+	H_2O	\rightarrow	H_3O^+	+	C	5.80×10^{-10}	$\text{cm}^3 \text{s}^{-1}$	47
C_2H_6^+	+	C_2H_4	\rightarrow	C_2H_4^+	+	C_2H_6	1.15×10^{-09}	$\text{cm}^3 \text{s}^{-1}$	47
C_2H_6^+	+	C_2H_2	\rightarrow	C_2H_5^+	+	C_2H_3	2.47×10^{-10}	$\text{cm}^3 \text{s}^{-1}$	47
C_2H_6^+	+	H	\rightarrow	C_2H_5^+	+	H_2	1.00×10^{-10}	$\text{cm}^3 \text{s}^{-1}$	47
C_2H_6^+	+	H_2O	\rightarrow	H_3O^+	+	C_2H_5	2.95×10^{-09}	$\text{cm}^3 \text{s}^{-1}$	47
C_2H_5^+	+	H	\rightarrow	C_2H_4^+	+	H_2	1.00×10^{-11}	$\text{cm}^3 \text{s}^{-1}$	47
C_2H_5^+	+	H_2O	\rightarrow	H_3O^+	+	C_2H_4	1.40×10^{-09}	$\text{cm}^3 \text{s}^{-1}$	47
C_2H_4^+	+	C_2H_3	\rightarrow	C_2H_5^+	+	C_2H_2	5.00×10^{-10}	$\text{cm}^3 \text{s}^{-1}$	47
C_2H_4^+	+	C_2H_3	\rightarrow	C_2H_3^+	+	C_2H_4	5.00×10^{-10}	$\text{cm}^3 \text{s}^{-1}$	47
C_2H_4^+	+	H	\rightarrow	C_2H_3^+	+	H_2	3.00×10^{-10}	$\text{cm}^3 \text{s}^{-1}$	47
C_2H_4^+	+	O	\rightarrow	CH_3^+	+	CHO	1.08×10^{-10}	$\text{cm}^3 \text{s}^{-1}$	47
C_2H_3^+	+	C_2H_6	\rightarrow	C_2H_5^+	+	C_2H_4	2.91×10^{-10}	$\text{cm}^3 \text{s}^{-1}$	47
C_2H_3^+	+	C_2H_4	\rightarrow	C_2H_5^+	+	C_2H_2	8.90×10^{-10}	$\text{cm}^3 \text{s}^{-1}$	47
C_2H_3^+	+	C_2H_3	\rightarrow	C_2H_5^+	+	C_2H	5.00×10^{-10}	$\text{cm}^3 \text{s}^{-1}$	47
C_2H_3^+	+	C_2H	\rightarrow	C_2H_2^+	+	C_2H_2	3.30×10^{-10}	$\text{cm}^3 \text{s}^{-1}$	47
C_2H_3^+	+	H	\rightarrow	C_2H_2^+	+	H_2	6.80×10^{-11}	$\text{cm}^3 \text{s}^{-1}$	47
C_2H_3^+	+	H_2O	\rightarrow	H_3O^+	+	C_2H_2	1.11×10^{-09}	$\text{cm}^3 \text{s}^{-1}$	47
C_2H_2^+	+	CH_4	\rightarrow	C_2H_3^+	+	CH_3	4.10×10^{-09}	$\text{cm}^3 \text{s}^{-1}$	50
C_2H_2^+	+	C_2H_6	\rightarrow	C_2H_5^+	+	C_2H_3	1.31×10^{-10}	$\text{cm}^3 \text{s}^{-1}$	48

$C_2H_2^+$	+	C_2H_6	\rightarrow	$C_2H_4^+$	+	C_2H_4	2.48×10^{-10}	$cm^3 s^{-1}$	47		
$C_2H_2^+$	+	C_2H_4	\rightarrow	$C_2H_4^+$	+	C_2H_2	4.14×10^{-10}	$cm^3 s^{-1}$	47		
$C_2H_2^+$	+	C_2H_3	\rightarrow	$C_2H_3^+$	+	C_2H_2	3.30×10^{-10}	$cm^3 s^{-1}$	47		
$C_2H_2^+$	+	H_2	\rightarrow	$C_2H_3^+$	+	H	1.00×10^{-11}	$cm^3 s^{-1}$	47		
$C_2H_2^+$	+	H_2O	\rightarrow	H_3O^+	+	C_2H	2.20×10^{-10}	$cm^3 s^{-1}$	47		
O_2^+	+	CH_2	\rightarrow	CH_2^+	+	O_2	4.30×10^{-10}	$cm^3 s^{-1}$	47		
O_2^+	+	CH	\rightarrow	CH^+	+	O_2	3.10×10^{-10}	$cm^3 s^{-1}$	47		
O_2^+	+	C_2H_4	\rightarrow	$C_2H_4^+$	+	O_2	6.80×10^{-10}	$cm^3 s^{-1}$	47		
O_2^+	+	C_2H_2	\rightarrow	$C_2H_2^+$	+	O_2	1.11×10^{-09}	$cm^3 s^{-1}$	47		
O_2^+	+	O^{\cdot}	\rightarrow	O	+	O_2	2.9×10^{-08}	$cm^3 s^{-1}$	51		
O_2^+	+	O^{\cdot}	\rightarrow	O	+	O	+	O	2.9×10^{-08}	$cm^3 s^{-1}$	51
O^{\cdot}	+	CH_4	\rightarrow	OH^{\cdot}	+	CH_3	1.00×10^{-10}	$cm^3 s^{-1}$	47		
O^{\cdot}	+	C	\rightarrow	CO	+	e^-	5.00×10^{-10}	$cm^3 s^{-1}$	47		
O^{\cdot}	+	H_2	\rightarrow	H_2O	+	e^-	7.00×10^{-10}	$cm^3 s^{-1}$	47		
O^{\cdot}	+	H_2	\rightarrow	OH^{\cdot}	+	H	3.00×10^{-11}	$cm^3 s^{-1}$	47		
O^{\cdot}	+	H	\rightarrow	OH	+	e^-	5.00×10^{-10}	$cm^3 s^{-1}$	47		
O^{\cdot}	+	O	\rightarrow	O_2	+	e^-	2.30×10^{-10}	$cm^3 s^{-1}$	51		
O^{\cdot}	+	O_2	\rightarrow	O	+	O_2	+	e^-	$k = f(E/N)$	10	
O^{\cdot}	+	CO	\rightarrow	CO_2	+	e^-	6.50×10^{-10}	$cm^3 s^{-1}$	47		
CO_2^+	+	CH_4	\rightarrow	CH_4^+	+	CO_2	5.50×10^{-10}	$cm^3 s^{-1}$	47		
CO_2^+	+	C_2H_4	\rightarrow	$C_2H_4^+$	+	CO_2	1.50×10^{-10}	$cm^3 s^{-1}$	47		
CO_2^+	+	C_2H_2	\rightarrow	$C_2H_2^+$	+	CO_2	7.30×10^{-10}	$cm^3 s^{-1}$	47		
CO_2^+	+	O_2	\rightarrow	O_2^+	+	CO_2	5.30×10^{-11}	$cm^3 s^{-1}$	47		
CO_2^+	+	O	\rightarrow	O_2^+	+	CO	1.64×10^{-10}	$cm^3 s^{-1}$	47		
H_3O^+	+	CH_2	\rightarrow	CH_3^+	+	H_2O	9.40×10^{-10}	$cm^3 s^{-1}$	47		
H_3O^+	+	CH	\rightarrow	CH_2^+	+	H_2O	6.80×10^{-10}	$cm^3 s^{-1}$	47		
H_3O^+	+	C_2H_3	\rightarrow	$C_2H_4^+$	+	H_2O	2.00×10^{-09}	$cm^3 s^{-1}$	47		
OH^{\cdot}	+	CH_3	\rightarrow	CH_3OH	+	e^-	1.00×10^{-09}	$cm^3 s^{-1}$	47		
OH^{\cdot}	+	CH	\rightarrow	CH_2O	+	e^-	5.00×10^{-10}	$cm^3 s^{-1}$	47		
OH^{\cdot}	+	C	\rightarrow	CHO	+	e^-	5.00×10^{-10}	$cm^3 s^{-1}$	47		
OH^{\cdot}	+	H	\rightarrow	H_2O	+	e^-	1.40×10^{-09}	$cm^3 s^{-1}$	47		

REFERENCES

- (1) Janev, R. K. *Atomic and Molecular Processes in Fusion Edge Plasmas*; Plenum Press: New York, 1995.
- (2) Janev, R. K.; Wang, J. G.; Murakami, I.; Kato, T. *National Institute for Fusion Science (NIFS) of Japan, Cross Sections and Rate Coefficients for Electron-Impact Ionization of Hydrocarbon Molecules*; Toki: Gifu, 2001.
- (3) Janev, R. K.; Reiter, D. Collision Processes of CH_y and CH_y⁺ Hydrocarbons with Plasma Electrons and Protons. *Phys. Plasmas* **2002**, *9* (9), 4071-4081.
- (4) Janev, R. K.; Reiter, D. Collision Processes of Hydrocarbon Species in Hydrogen Plasmas. Part 2. The Ethane and Propane Families. *ChemInform* **2003**, *34* (37), DOI: 10.1002/chin.200325274.
- (5) Janev, R. K.; Reiter, D. Collision Processes of Hydrocarbon Species in Hydrogen Plasmas. Part 2. The Ethane and Propane Families. *ChemInform* **2003**, *34* (37), DOI: 10.1002/chin.20033729.
- (6) Janev, R. K.; Reiter, D. Collision Processes of C_{2,3}H_y and C_{2,3}H_y⁺ Hydrocarbons with Electrons and Protons. *Phys. Plasmas* **2004**, *11* (2), 780-829.
- (7) Engelhardt, A. G.; Phelps, A. V. Elastic and Inelastic Collision Cross Sections in Hydrogen and Deuterium from Transport Coefficients. *Phys. Rev.* **1963**, *131* (5), 2115-2128.

- (8) Trajmar, S.; Register, D. F.; Chutjian, A. Electron Scattering By Molecules II. Experimental Methods and Data. *Phys. Rep.* **1983**, *97* (5), 219-356.
- (9) Corrigan, S. J. B. Dissociation of Molecular Hydrogen by Electron Impact. *J. Chem. Phys.* **1965**, *43* (12), 4381-4386.
- (10) Eliasson, B.; Hirth, M.; Kogelschatz, U. Ozone Synthesis From Oxygen in Dielectric Barrier Discharges. *J. Phys. D Appl. Phys.* **1987**, *20* (11), 1421-1437.
- (11) Lawton, S. A.; Phelps, A. V. Excitation of the b $1\Sigma^+g$ State of O₂ By Low Energy Electrons. *J. Chem. Phys.* **1978**, *69* (3), 1055-1068.
- (12) Joshipura, K. N.; Patel, P. M. Cross Sections of e⁻-O Scattering at Intermediate and High Energies (E_i=8.7—1000 eV). *PhRvA* **1993**, *48* (3), 2464-2467.
- (13) Laher, R. R.; Gilmore, F. R. Updated Excitation and Ionization Cross Sections for Electron Impact on Atomic Oxygen. *J. Phys. Chem. Ref. Data* **1990**, *19* (1), 277-305.
- (14) Itikawa, Y. Cross Sections for Electron Collisions With Carbon Dioxide, *J. Phys. Chem. Ref. Data* **2002**, *31*, 749-767.
- (15) *Lxcat database* Website; <http://www.lxcat.laplace.univ-tlse.fr>.
- (16) Rapp, D.; Briglia, D. D. Total Cross Sections for Ionization and Attachment in Gases by Electron Impact. II. Negative-Ion Formation. *J. Chem. Phys.* **1965**, *43* (5), 1480-1489.
- (17) McConkey, J. W.; Malone, C. P.; Johnson, P. V.; Winstead, C.; McKoy, V.; Kanik, I. Electron Impact Dissociation of Oxygen-Containing Molecules—A Critical Review. *Phys. Rep.* **2008**, *466* (1-3), 1103.

- (18) Itikawa, Y.; Mason, N. Cross Sections for Electron Collisions with Water Molecules. *J. Phys. Chem. Ref. Data* **2005**, *34* (1), 122.
- (19) Riahi, R.; Teulet, P.; Ben Lakhdar, Z.; Gleizes, A. Cross-Section and Rate Coefficient Calculation for Electron Impact Excitation, Ionisation and Dissociation of H and OH Molecules. *EPJD* **2006**, *40* (2), 223-230.
- (20) Florescu-Mitchell, A. I.; Mitchell, J. B. A. Dissociative Recombination. *Phys. Rep.* **2006**, *430* (5-6), 277-374.
- (21) Kossyi, I. A.; Kostinsky, A. Y.; Matveyev, A. A.; Silakov, V. P. Kinetic Scheme of the Non-Equilibrium Discharge in Nitrogen-Oxygen Mixtures. *Plasma Sources Sci. T.* **1992**, *1* (3), 207-220.
- (22) Tsang, W.; Hampson, R. F. Chemical Kinetic Data Base for Combustion Chemistry. Part I. Methane and Related Compounds. *J. Phys. Chem. Ref. Data* **1986**, *15* (3), 1087-1279.
- (23) Baulch, D. L.; Cobos, C. J.; Cox, R. A.; Esser, C.; Frank, P.; Just, T.; Kerr, J. A.; Pilling, M. J.; Troe, J.; Walker, R. W.; Warnatz, J. Evaluated Kinetic Data for Combustion Modelling. *J. Phys. Chem. Ref. Data* **1992**, *21* (3), 411-734.
- (24) Tsang, W. Chemical Kinetic Data Base for Combustion Chemistry. Part 3: Propane. *J. Phys. Chem. Ref. Data* **1988**, *17* (2), 887-951.

- (25) Stewart, P. H.; Larson, C. W.; Golden, D. M. Pressure and Temperature Dependence of Reactions Proceeding Via a Bound Complex. 2. Application to $2\text{CH}_3 \rightarrow \text{C}_2\text{H}_5 + \text{H}$. *Combust. Flame* **1989**, *75* (1), 25-31.
- (26) Laufer, A. H.; Fahr, A. Reactions and Kinetics of Unsaturated C₂ Hydrocarbon Radicals. *Chem. Rev.* **2004**, *104* (6), 2813-2832.
- (27) Harding, L. B.; Guadagnini, R.; Schatz, G. C. Theoretical Studies of the Reactions Hydrogen Atom + Methylidyne \rightarrow carbon + Hydrogen and Carbon + Hydrogen \rightarrow Methylene Using an Ab Initio Global Ground-State Potential Surface for Methylene. *J. Phys. Chem.* **1993**, *97* (21), 5472-5481.
- (28) Lin, S. Y.; Guo, H. Case Study of a Prototypical Elementary Insertion Reaction: $\text{C}(1\text{D}) + \text{H}_2 \rightarrow \text{CH} + \text{H}$. *J. Phys. Chem. A* **2004**, *108*, 10066-10071.
- (29) Harding, L. B.; Georgievskii, Y.; Klippenstein, S. J. Predictive Theory for Hydrogen Atom – Hydrocarbon Radical Association Kinetics. *J. Phys. Chem. A* **2005**, *109* (21), 4646-4656.
- (30) Baulch, D. L.; Cobos, C. J.; Cox, R. A.; Frank, P.; Hayman, G.; Just, T.; Kerr, J. A.; Murrells, T.; Pilling, M. J.; Troe, J.; Walker, R. W.; Warnatz, J. Evaluated Kinetic Data for Combustion Modeling. Supplement I. *J. Phys. Chem. Ref. Data* **1994**, *23*, 847-848.
- (31) Tsang, W. Chemical Kinetic Data Base for Combustion Chemistry Part V. Propene. *J. Phys. Chem. Ref. Data* **1991**, *20* (2), 221-273.

- (32) Hadj-Ziane, S.; Held, B.; Pignolet, P.; Peyrous, R.; Coste, C. Ozone Generation in an Oxygen-Fed Wire-to-Cylinder Ozonizer at Atmospheric Pressure. *J. Phys. D Appl. Phys.* **1992**, *25* (4), 677-685.
- (33) Baulch, D. L.; Bowman, C. T.; Cobos, C. J.; Cox, R. A.; Just, T.; Kerr, J. A.; Pilling, M. J.; Stocker, D.; Troe, J.; Tsang, W.; Walker, R. W.; Warnatz, J. Evaluated Kinetic Data for Combustion Modeling: Supplement II. *J. Phys. Chem. Ref. Data* **2005**, *34*, 757-1397.
- (34) Fang, D. C.; Fu, X. Y. CASSCF and CAS+1+2 Studies on the Potential Energy Surface and the Rate Constants for the Reactions between CH₂ and O₂. *J. Phys. Chem. A* **2002**, *106*, 2988-2993.
- (35) Dean, A. J.; Davidson, D. F.; Hanson, R. K. A Shock Tube Study of Reactions of Carbon Atoms with Hydrogen and Oxygen Using Excimer Photolysis of C₃O₂ and Carbon Atom Atomic Resonance Absorption Spectroscopy. *J. Phys. Chem.* **1991**, *95* (1), 183-191.
- (36) Atkinson, R.; Baulch, D. L.; Cox, R. A.; Crowley, J. N.; Hampson, R. F.; Hynes, R. G.; Jenkin, M. E.; Rossi, M. J.; Troe, J. Evaluated Kinetic and Photochemical Data for Atmospheric Chemistry: Volume II – Gas Phase Reactions of Organic Species. *Atmos. Chem. Phys.* **2006**, *6*, 3625-4055.
- (37) Atkinson, R.; Baulch, D. L.; Cox, R. A.; Crowley, J. N.; Hampson, R. F.; Hynes, R. G.; Jenkin, M. E.; Rossi, M. J.; Troe, J. Evaluated Kinetic and Photochemical Data for Atmospheric Chemistry: Volume I - Gas Phase Reactions of Ox, HO_x, NO_x and SO_x. *Atmos. Chem. Phys.* **2004**, *4*, 1410-1738.

- (38) Pereira, R. D.; Baulch, D. L.; Pilling, M. J.; Robertson, S. H.; Zeng, G. Temperature and Pressure Dependence of the Multichannel Rate Coefficients for the CH₃+ OH System. *J. Phys. Chem. A* **1997**, *101* (50), 9681-9693.
- (39) Sun, H.; Tang, Y. Z.; Wang, Z. L.; Pan, X. M.; Li, Z. S.; Wang, R. S. DFT Investigation of the Mechanism of CH₂CO + O(3P) Reaction. *IJQC* **2005**, *105*, 527-532.
- (40) Kuwata, K. T.; Hasson, A. S.; Dickinson, R. V.; Petersen, E. B.; Valin, L. C. Quantum Chemical and Master Equation Simulations of the Oxidation and Isomerization of Vinyloxy Radicals. *J. Phys. Chem. A* **2005**, *109*, 2514-2524.
- (41) Delbos, E.; Fittschen, C.; Hippler, H.; Krasteva, N.; Olzmann, M.; Viskolcz, B. Rate Coefficients and Equilibrium Constant for the CH₂CHO + O₂ Reaction System *J. Phys. Chem. A* **2006**, *110*, 3238-3245.
- (42) Jodkowski, J. T.; Rayez, M. T.; Rayez, J. C.; Berces, T.; Dobe, S. Theoretical Study of the Kinetics of the Hydrogen Abstraction from Methanol. 3. Reaction of Methanol with Hydrogen Atom, Methyl, and Hydroxyl Radicals. *J. Phys. Chem. A* **1999**, *103*, 3750-3765.
- (43) Hou, H.; Wang, B. S.; Gu, Y. S. Mechanism of the OH + CH₂CO Reaction. *Phys. Chem. Chem. Phys.* **2000**, *2*, 2329-2334.
- (44) Tsang, W. Chemical Kinetic Data Base for Combustion Chemistry. Part 2. Methanol. *J. Phys. Chem. Ref. Data* **1987**, *16*, 471-508.

- (45) Jasper, A. W.; Klippenstein, S. J.; Harding, L. B.; Ruscic, B. Kinetics of the Reaction of Methyl radical with Hydroxyl Radical and Methanol Decomposition. *J. Phys. Chem. A* **2007**, *111* (19), 3932-3950.
- (46) Lu, C. W.; Chou, S. L.; Lee, Y. P.; Xu, S. C.; Xu, Z. F.; Lin, M. C. J. Experimental and Theoretical Studies of Rate Coefficients for the Reaction O(3P)+CH₃OH at High Temperatures. *Chem. Phys.* **2005**, *122* (24), 244-314.
- (47) Woodall, J.; Agúndez, M.; Markwick-Kemper, A. J.; Millar, T. J. The UMIST Database for Astrochemistry 2006. *Astron. Astrophys.* **2007**, *466* (3), 1197-1204.
- (48) Kim, Y. H.; Fox, J. L. The Chemistry of Hydrocarbon Ions in the Jovian Ionosphere. *Icarus* **1994**, *112* (2), 310-325.
- (49) Tahara, H.; Minami, K.; Murai, A.; Yasui, T.; Yoshikawa, T. Diagnostic Experiment and Kinetic Model Analysis of Microwave CH₄/H₂ Plasmas for Deposition of Diamondlike Carbon Films. *Jpn. J. Appl. Phys. 1* **1995**, *34*, 1972-1779.
- (50) Tachibana, K.; Nishida, M.; Harima, H.; Urano, Y. Diagnostics and Modeling of a Methane Plasma Used in the Chemical Vapour Deposition of Amorphous Carbon Films. *J. Phys. D Appl. Phys.* **1984**, *17* (8), 1727-1742.
- (51) Gudmundsson, J. T.; Thorsteinsson, E. G. Oxygen Discharges Diluted with Argon: Dissociation Processes. *Plasma Sources Sci. T.* **2007**, *16*, 399-412.